Czech Technical University in Prague
Faculty of Nuclear Sciences and Physical Engineering

Department of Physics

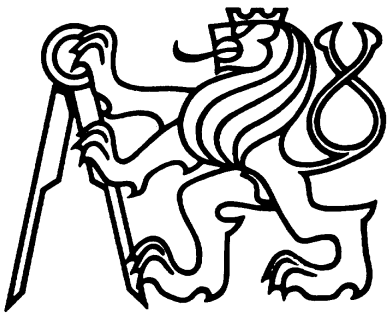

Bottom quark charge identification using muons in jets

Research Project

Bc. Lukáš Novotný

Supervisor: Ing. Michal Marčišovský, PhD.

Prague, 2017

České vysoké učení technické v Praze
Fakulta jaderná a fyzikálně inženýrská

Katedra fyziky

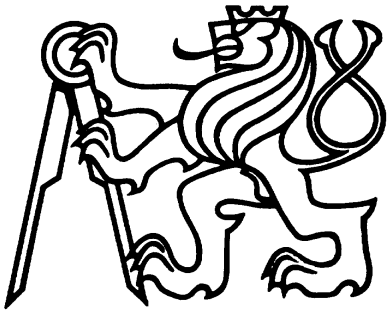

Identifikace náboje bottom kvarků prostřednictvím vlastností mionů v jetech

Výzkumný úkol

Bc. Lukáš Novotný
Vedoucí práce: Ing. Michal Marčišovský, PhD.
Praha, 2017

Zadání práce

Declaration

I hereby declare that this project is the result of my own work and all the sources I used are in the list of references. I have no objection to usage of this work in compliance with the act §60 Law No. 121/2000 Coll. (Copyright Act), and with the rights connected with the copyright act including the changes in the act.

Prohlášení

Prohlašuji, že jsem tuto práci vypracoval samostatně a použil jsem pouze podklady uvedené v přiloženém seznamu. Nemám závažný důvod proti použití tohoto díla ve smyslu §60 zákona č.121/2000 Sb., o právu autorském, o právech souvisejících s právem autorským a o změně některých zákonů (autorský zákon).

v Praze dne ....

Lukáš Novotný

Acknowledgement

I would like to express my gratitude to my supervisor Michal Marčišovský for his invaluable advice, patience, willingness and professional guidance during the realization of this work. I am very grateful to Mária Marčišovská for language corrections and to Václav Vrba for overall support of my work. Furthermore, I would like to thank James William Walder, Adam Edward Barton and Vladimir Nikolaenko for preparing the data sample and helping with data analysis. I am very grateful to Mária Smižanská for her helpful advices and discussions. Last but not least, I would like to thank my family, girlfriend and friends for their encouragement and support.

Lukáš Novotný

Title: **Bottom quark charge identification using muons in jets**

Author: Lukáš Novotný

Specialization: Experimental nuclear and particle physics

Sort of project: Research project

Supervisor: Ing. Michal Marčišovský, PhD.

Abstract: This thesis is dedicated to the study of the tag power and tag probability of a B^+ meson, which is used as the calibration tool in $B_s^0 \to J/\psi\phi$ opposite side tagging. For this purpose, the whole 2016 data recorded by the detector ATLAS at LHC are used. In this work, firstly the Standard Model with emphasis on the CKM formalism is introduced, followed by the theoretical background of $B_s^0 - \bar{B}_s^0$ mixing in the $B_s^0 \to J/\psi\phi$ decay mode. Then, the ATLAS trigger system and offline software is presented. The thesis ends with the data analysis model and results.

Key words: $B^{\pm}$, B_s^0, B physics, CP violation, tag power, tag probability, ATLAS, LHC

Název práce: **Identifikace náboje bottom kvarků prostřednictvím vlastností mionů v jetech**

Autor: Lukáš Novotný

Obor: Experimentální jaderná a částicová fyzika

Druh práce: Výzkumný úkol

Vedoucí práce: Ing. Michal Marčišovský, PhD.

Abstrakt: Tato práce se věnuje tagování mezonu B^+, jehož tagovací pravděpodobnost je použita pro kalibraci tagování mezonu $B_s^0 \to J/\psi\phi$. Pro tento účel byla použita data z pp srážek získaná detektorem ATLAS v LHC v roce 2016.
Zpočátku se práce věnuje Standardnímu modelu s důrazem na CKM formalismus. Následuje teoretický popis CP narušení v mísení $B_s^0 - \bar{B}_s^0$. Poté je popsán systém triggerování a offline software na detektoru ATLAS. Na závěr je ukázán analyzační model a získané výsledky analýzy.

Klíčová slova: $B^{\pm}$, B_s^0, B fyzika, CP narušení, síla taggování, pravděpodobnost tagování, ALTAS, LHC

Contents

List of Figures

List of Tables

Introduction

The CP-violating phase ϕ_s arises in the interference between the amplitudes of B_s^0 mesons decaying via $b \to s$ transitions and those decaying after oscillation. The flavour tagging has large impact on studies of the ϕ_s phase, especially for the opposite side tagging.
To study and calibrate this tagging, the decay, where the sign of B meson is known, is used.
This research task is organised as follows: The first chapter gives a brief overview of the Standard Model, paying particular attention to the concepts surrounding discrete symmetries and CKM formalism.
The second chapter is dedicated to the theoretical background of the $B_s^0 - \bar{B}_s^0$ mixing. The B meson properties are followed by $B_s^0 - \bar{B}_s^0$ mixing overview in the $B_s^0 \to J/\psi\phi$ decay mode. The difference between flavour and mass eigenstates is described there, leading to the measured differential branching ratio in terms of transversality formalism. Previous measurements of $\mathcal{CP}$ violation at D0, LHCb and ATLAS detectors are briefly mentioned at the end of this chapter.
Third chapter introduces the ATLAS trigger system and the offline software. The muon reconstruction is described here, dividing muons into groups according the hit information input for the reconstruction algorithms and their quality of reconstruction. The software used in this analysis is also described there, namely ROOT, RooFit and sPlot.
The main part topic goal of this work is presented in the last chapter, where the analysis initial steps are discussed, such as the candidate reconstruction and the determination of the selection cut. The results of $B^{\pm} \to J/\psi K^{\pm}$ mass fit are mentioned here, followed by the description of the sideband subtraction method. Single muon tagging and cone charge tagging results with respect to the cuts and parameters variations. The partial resulting observables employed in the construction of the tag variables, which are used in the tagging of the B_s^0 decay, are referred at the end of this chapter.

Chapter 1

Introduction to the particle physics

Contemporary instrumentation and theoretical models allow us to describe the behaviour of world on the particle level. These objects and their interactions are described by the Standard Model of particles and fields. According to this model, all matter is made of particles without inner structure, called elementary particles, and interacts through force carriers.

family		symbol	name	mass	spin	charge
fermions	quarks	u	up	$2.3^{+0.7}_{-0.5}$ MeV	1/2	2/3
		d	down	$4.8^{+0.5}_{-0.3}$ MeV	1/2	$-1/3$
		s	strange	95 ± 5 MeV	1/2	$-1/3$
		c	charm	1.275 ± 0.025 GeV	1/2	2/3
		b	bottom	4.18 ± 0.03 GeV	1/2	$-1/3$
		t	top	$173.21 \pm 0.51 \pm 0.71$ GeV	1/2	2/3
	leptons	e	electron	510.998928 ± 0.000011 keV	1/2	-1
		μ	muon	$105.6583715 \pm 0.0000035$ MeV	1/2	-1
		τ	tau	1776.82 ± 0.16 MeV	1/2	-1
		ν_e	e-neutrino	< 2 eV	1/2	0
		ν_μ	μ-neutrino	< 0.19 MeV	1/2	0
		ν_τ	τ-neutrino	< 18.2 MeV	1/2	0
bosons	vector	γ	photon	$< 10^{-18}$ eV	1	0
		g	gluon	0	1	0
		$W^\pm$	W boson	80.385 ± 0.015 GeV	1	± 1
		Z^0	Z boson	91.1876 ± 0.0021 GeV	1	0
	scalar	H	Higgs boson	125.7 ± 0.4 GeV	0	0

Table 1.1: Particles (6 quarks and 6 leptons) and force carriers (5 bosons) in the Standard model [1].

1.1 The Standard model

This theory, developed in the 1970s, successfully explains collider experimental results. It contains bosons with integer fundamental spin and 12 fermions with half-integer fundamental spin. Fermions obey Fermi-Dirac statistics and bosons obey Bose-Einstein statistics. For more details, see Table 1.1.

1.1.1 Fundamental interactions

	gravitational	electromagnetic	weak	strong
boson	graviton[1]	photon	$W^{\pm}$, Z^0	gluons
spin-parity	2^+	1^-	1^-, 1^+	1^-
mass [GeV/c^2]	0^2	0	$m_W = 80.2$, $m_Z = 91.2$	0
source	mass	electric charge	weak charge	colour charge
range [m]	∞	∞	10^{-18}	$\leq 10^{-15}$
coupling constant	$\frac{G_N M^2}{4\pi\hbar c} = 5 \cdot 10^{-40}$	$\alpha = \frac{e^2}{4\pi\hbar c} = \frac{1}{137}$	$\frac{G\left(Mc^2\right)^2}{(\hbar c)^3} = 1 \cdot 10^{-5}$	$\alpha_S \lesssim 1$

Table 1.2: Fundamental interactions [2].

There are four fundamental interactions - strong, electromagnetic, weak and gravitational, but only the first three are incorporated into the Standard Model and are mediated by gauge bosons mentioned in Table 1.1. In our everyday macroscopic and mundane life, the gravitational and electromagnetic forces are usually observed, strong and weak interaction become important at the distance scales of 10^{-15} m and smaller.

Electromagnetic interactions

Electromagnetic interactions between charged particles are mediated by a photon exchange. Particles with the same sign of electric charge repel each other and particles with the opposite charge attract each other. The value of the coupling constant, or the fine structure constant, is at low energy limits equal to:

$$\alpha = \frac{1}{4\pi\varepsilon_0}\frac{e^2}{\hbar c} \simeq \frac{1}{137}, \tag{1.1}$$

where e is the elementary charge, c is speed of light and ε is vacuum permeability. At the energy scales of Z^0 boson mass, the coupling constant is $\alpha \simeq \frac{1}{128}$. The lightest charged

[1]The graviton is a hypothetical particle, which is not included in the Standard Model, because quantum gravity theory has not been invented. However, the gravitational waves (pertubations in linearized spacetime) were observed in 2016 [3].

[2]The mass of graviton is expected to be zero in four dimensions (three space and one time), but it can have nonzero mass in more dimensions.

particle is an electron with a lifetime $\tau_e > 4 \cdot 10^{26}$ years. Because electron can decay only by violating the charge conservation law and since it has not been observed, it is assumed, that in every interaction or decay, the total charge is conserved. The electromagnetic interaction is described within the quantum electrodynamics framework (QED). In this theory, the definition (1.1) is not constant, but it depends on the energy scale at which the measurement is made..

Gravitational interaction

The effects of the gravitational interaction demonstrate themselves predominantly in the macroscopic world and at large spatial scales, gravitating objects curve the spacetime around themselves. This curvature can manifest itself by exerting a force on a nearby objects. It binds objects to the surface of the Earth, holds together star clusters and galaxies. Its coupling strength is defined via the Newtonian constant

$$G = 6.673 \cdot 10^{-11}\ \mathrm{m^3 kg^{-1} s^{-2}}, \tag{1.2}$$

which is a constant used in the Einstein field equations of the general theory of relativity:

$$R_{\mu\nu} - \frac{1}{2} R g_{\mu\nu} = \frac{8\pi G}{c^4} T_{\mu\nu}, \tag{1.3}$$

where $R_{\mu\nu}$ is the Ricci curvature tensor, R is the scalar curvature (the Ricci scalar), $g_{\mu\nu}$ is the metric tensor and $T_{\mu\nu}$ is the stress-energy tensor generalizing the stress tensor of Newtonian physics [4].
In the Newtonian approach, the magnitude of the force between two point particles with mass M and distance r is given by $\frac{G_N M^2}{r^2}$. When calculating the electromagnetic force between charged particles, e^2/r^2, we can substitute GM^2 in the definition (1.1) for e^2/ε_0 and obtain a constant

$$\frac{GM^2}{4\pi\hbar c} = 5.34 \cdot 10^{-40}. \tag{1.4}$$

which demonstrates the the relative strength of the gravity to other forces. In comparison with the fine structure constant (1.1), the gravitational interaction is negligibly small in the high energy physics and microscopic physics and it is not included in the Standard Model. On the other hand, gravitational interaction is crucial at large spatial scales such as in cosmology, because it is a long-distance interaction and non-existence of negative gravitational charge.
The gravitational force is only attractive and it is hypothetically mediated through graviton in the quantum field theories [5], the massless (in four dimensions) particle with spin 2. As mentioned in the footnote of the Table 1.2, the gravitational waves were recently observed, but the graviton has not been observed.

Strong interaction

Unlike leptons, quarks and gluons interact via the strong interaction. This force is responsible for binding quarks and gluons together, forming mesons and baryons (and other

exotic states like tetraquarks and pentaquarks). In order for quarks in baryons to not violate Pauli exclusion principle, the color quantum number has been introduced as an extra degree of freedom in the quark model. Every quark has either red (r), blue (b) or green (g) colour. Similarly, antiquarks have their anticolour (antired - $\bar{r}$, antiblue - $\bar{b}$ or antigreen $\bar{g}$). Mediators of strong interaction carrying one colour and one anticolour, gluons, are postulated to belong the an octet state and one colour singlet. The representation of the octet can be composed of the combinations:

$$r\bar{g},\ r\bar{b},\ g\bar{r},\ g\bar{b},\ b\bar{r},\ b\bar{g},\ \frac{1}{\sqrt{2}}(r\bar{r}-b\bar{b}),\ \frac{1}{\sqrt{6}}(r\bar{r}+b\bar{b}-g\bar{g})$$

The gluon colour singlet state $\frac{1}{\sqrt{3}}(r\bar{r}+b\bar{b}+g\bar{g})$ does not carry the net colour.
The strong interaction is described within the quantum chromodynamics framework (QCD).

Weak interaction

The weak interaction is mediated through exchange of $W^{\pm}$ or Z^0 bosons (Z^0 is considered to mediate the electroweak interaction, because due to its quantum numbers it can mix with the photon [2]). This interaction between quarks and leptons can be encountered in macroscopic world. It is for example responsible for thermonuclear fusion in Sun or for beta decay, where one neutron in the nucleus is transformed into proton while radiating the virtual W^- boson, which subsequently decays into electron and electron antineutrino (Fig. 1.1). As it is demonstrated on this reaction, the charged weak interaction changes flavour. It also has the shortest range of interaction, see Table 1.2.

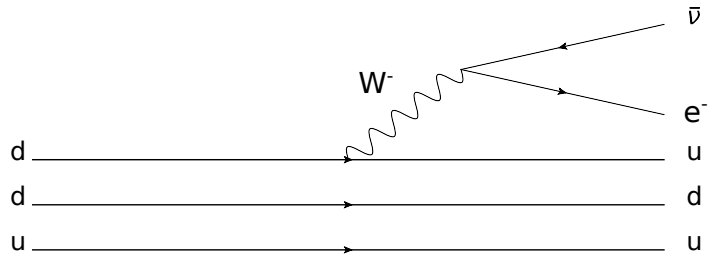

Figure 1.1: The neutron (valence quarks ddu) decaying into the proton (valence quarksudu), electron and electron antineutrino via the weak interaction.

1.1.2 Leptons

Nowadays, six leptons are known to exist. There are three leptons with charge equal to -1: electron e, muon μ and tau τ. To each charged lepton there is its neutral counterpart, called neutrino and it is labelled ν, one for each charged lepton. Each charged lepton together with its neutrino forms one generation, electron belongs to the first generation, muon to the second and tauon to the third.
The behaviour of leptons in the reaction can be described by lepton flavour numbers L_e,

L_μ, L_τ, equal to +1 for each lepton and −1 for each antilepton. All lepton flavour numbers have to be conserved in the process through arbitrary fundamental interaction.
The muon and tau are unlike electron unstable, their mean lifetimes are $t_\mu = 2.197 \cdot 10^{-6}$ s for μ [1] and $t_\tau = 2.9 \cdot 10^{-13}$ s for τ [1] respectively.
All leptons have spin 1/2 and interact weakly, but only charged leptons interact electromagnetically. Thus, neutrinos can pass through the ordinary matter more easily than other leptons. They were originally postulated in 1930 by Wolfgang Pauli[6] in order to conserve the energy and momentum in the β-decay. It is assumed in the Standard Model that neutrinos are massless, however neutrino flavour mixing and flavour oscillations have been observed, which implicates that neutrinos are not massless particles [3] and the Standard Model is incomplete.

1.1.3 Quarks

Similarly to leptons, quarks have spin 1/2 and form three doublets

$$\begin{pmatrix} u \\ d \end{pmatrix}, \begin{pmatrix} s \\ c \end{pmatrix}, \begin{pmatrix} t \\ b \end{pmatrix}. \tag{1.5}$$

Quarks u and d form the first, s and c the second and t and b the third generation. The upper part of doublets has electric charge 2/3 (u, c and t) and the bottom part has charge of −1/3 (d, s and b). Quarks interact through all known fundamental forces, and are the only ones which do through strong force, because they carry one of three colours, red (r), green (g) and (b).
The existence of quarks was independently postulated in 1964 by G. Zweig [8] and M. Gell-Mann [9]. Only up, down and strange quarks were known at the time. Other quarks were discovered later, charm quark in 1974 [10], bottom quark in 1977 [11] and top quark in 1995 [12].
Quarks can exist only in a bound state with another quarks or antiquarks, separate single quark has not been observed, except for the top quark, which decays before it has a chance to hadronize. Quark composites are called hadrons, the most common are mesons and baryons, but recently also tetraquarks and pentaquarks have been observed. Nevertheless, the bound state of the top quark was not observed due to its small lifetime $\tau = 5 \cdot 10^{-25}$ s.
There are quantum numbers which describe quarks and their formations. The baryon number $\mathfrak{B}$ is defined as the number of baryons minus number of antibaryons,

$$\mathfrak{B} = N(\text{baryons}) - N(\text{antibaryons}).$$

Mesons have baryon number $\mathfrak{B} = 0$ and are bosons, because with given spin of quarks $\frac{1}{2}$, their total spin is either 0 or 1. They are bound states of quark q and antiquark $\overline{q}$, where flavour of q and $\overline{q}$ can be different.

[3] Masses of neutrino are estimated in the Table 1.1. According to precise cosmological measurement of Planck probe, the sum of neutrino masses is $\sum m_\nu < 0.23$ eV. [13]

Baryons are bound state of three quarks. They are fermions (the total spin is a multiple of half integer) and their baryon number is $\mathfrak{B} = 1$ ($\mathfrak{B} = -1$ for antibaryons). Our world is primarily made of baryons with u and d quarks. The most common baryons are proton (uud) and neutron (udd), which form the nucleus of each atom.

Tetraquarks and pentaquarks - new structures of quarks and antiquarks have been recently observed, which cannot be classified either as meson or baryons. In 2007, the observation of the $Z(4430)$ state, a $c\bar{c}d\bar{u}$ tetraquark candidate, was announced by the Belle experiment in Japan. The existence of $Z(4430)$ was confirmed in 2014 at the LHCb experiment[14].
After this observation, it is not surprising, that also pentaquark state was observed, namely the $J/\psi p$ resonance in $\Lambda_b^0 \to J/\psi K^- p$ decays.[15] The quark content of this pentaquark is expected to be $c\bar{c}uud$.

1.1.4 Antiparticles

The existence of antiparticles was predicted originally in 1929 by Paul Dirac [16]. Antiparticles are objects with the same mass as the corresponding particles (fermions and bosons), but they have opposite sign of electric and colour charge. According to Dirac, the vacuum consists of sea (often called Dirac sea), where negative energy levels are possible[4]. By transferring the energy $E > 2m_0c^2$ to the negative energy electron, it can be lifted into the positive energy state, from which electron and its antiparticle positron can be created. The energy transferred to e^+e^- creation can be considered as the energy of γ-ray in the presence of the nucleus. The opposite process is also possible, an e^+e^- bound state, called positronium, can annihilate into two or three γ-rays, but not to a single γ-particle, due to the total momentum conservation.
The first antiparticle (positron) was discovered in 1932 in a cloud chamber exposed to cosmic rays.
Later, other antiparticles were discovered. Not all particles have its antipartner, for example, the boson Z^0 or γ is particle and its own antiparticle simultaneously.

1.2 Symmetries

In physics, the motion equations are determined from the Lagrangian of the given system. This Lagrangian is dependent on several variables (like space position, angles, vector of momentum or angular momentum).

[4]Negative energies may occur in quantum mechanics and are included in the relativistic relation $E = \pm\sqrt{p^2c^2 + m^2c^4}$.

Property	Symmetry	Conserved quantity
homogeneity of time	time translation	energy
homogeneity of space	space translation	momentum
isotropy of space	space rotation	angular momentum

Table 1.3: Examples of the continuous symmetries and their conserved quantities.

Applying a transformation (e. g. Lorentz or Galilean transformation), Euler-Lagrange equations for given Lagrangian can be same as they have been before the transformation. In this case, the system is invariant under the transformation and for every symmetry of a Lagrangian there exists a conserved quantity called the constant of motion. Examples of symmetries and their conserved quantities are in the Table 1.3. In this table, only continuous symmetries are discussed, but also discrete symmetries exists, which are subject of the next section.

1.2.1 Discrete symmetries

In quantum mechanics the state of a physical system is described by a ray $|\psi\rangle$ in a Hilbert space. The time dependent system (non-relativistic case) is described by the Schrödinger equation

$$\imath\hbar\frac{\partial}{\partial t}|\psi\rangle = \hat{\mathcal{H}}|\psi\rangle\,. \tag{1.6}$$

In this case, the Hamiltonian $\hat{\mathcal{H}}$ has discrete spectrum of eigenvalues. Other examples of discrete spectrum are squared angular momentum $\hat{\mathcal{L}}^2$ with eigenvalues $\sqrt{l(l+1)}\hbar$ ($l \in \mathbb{N}$) and the third component of angular momentum $\hat{\mathcal{L}}_z$ with eigenvalues $m\hbar$ ($m \in \mathbb{Z}$).
Special group of symmetries are represented by unitary or anti-unitary operators. The eigenvalues of these operators are 1 or -1. To this group belong operators important for the next chapters, the parity operator $\hat{\mathcal{P}}$, charge conjugation operator $\hat{\mathcal{C}}$ and time reversal operator $\hat{\mathcal{T}}$.

The parity

The parity or space inversion operation converts a right handed coordinate system to left handed $(x, y, z \to -x, -y, -z)$

$$\hat{\mathcal{P}}\psi(\mathbf{r}) = \psi(-\mathbf{r})\,. \tag{1.7}$$

Moreover, it also inverses the direction of momentum, but it does not change time and angular momentum. In two dimension, the inversion of axes is equivalent to the 180° rotation.
Applying twice the parity operator, the original state is obtained, which implies that the eigenvalues of the parity are ± 1.
Parity conservation implies that any physical process will proceed identically when viewed

in mirror image.
The parity had seemed to be conserved in every decay until 1956, when Wu observed an parity violation in ^{60}Co decay [17]. The cobalt nuclei was placed in the magnetic field and then the counting rate was detected in dependence of angle. By inverting the magnetic field direction and thus the polarisation of the cobalt nucleus, a difference in counting rate could be detected. However, the overall counting rate does not change, which means the parity was violated.

The charge conjugation

The charge conjugation operator $\hat{\mathcal{C}}$ changes the sign of the all quantum charges and does not affect the mass, linear momentum and spin of the particle. This means that the operator $\hat{\mathcal{C}}$ transform the particle into antiparticle,

$$\hat{\mathcal{C}}\psi\left(\mathbf{r}\right) = \bar{\psi}\left(\mathbf{r}\right) \tag{1.8}$$

This operator is similarly to parity conserved in electromagnetic and strong interactions and violated in weak interactions. The charge conjugation is violated in the transformation of left-handed neutrino into the left-handed anti-neutrino, which was not observed[5].

The time reversal

The time reversal operator $\hat{\mathcal{T}}$ changes the time direction,

$$\hat{\mathcal{T}}\psi\left(\mathbf{r},t\right) = \bar{\psi}\left(\mathbf{r},-t\right). \tag{1.9}$$

Because $\mathcal{CP}$ symmetry is violated and $\mathcal{CPT}$ symmetry is not violated, the time reverse has to be also violated. The first direct observation of the T-symmetry violation was made at CERN LEAR ring in 1998 [18].

$\mathcal{CPT}$ invariance

The $\mathcal{CPT}$ theorem states that all interactions are invariant under the simultaneous application of the parity, charge conjugation and time reversal operators. Using the charge conjugation $\mathcal{C}$ operator independently, it would be observed to be violated in the weak interactions. $\mathcal{CP}$ is also violated (thus the time $\mathcal{T}$ is violated). This violation was firstly observed in the neutral kaon decay [19]. The $\mathcal{CPT}$ invariance in the observations of the high energy physics experiments seems to be conserved [20],[21],[22].

1.2.2 $\mathcal{CP}$ violation

As discussed in section 1.2.1, the parity $\mathcal{P}$ is violated. The first observation of this violation has been made in 1956 by Wu. If $\mathcal{CP}$ were an exact symmetry, the laws of Nature would

[5]There exist only left-handed neutrino and right-handed anti-neutrino using the Dirac description of neutrinos

be the same for matter and for antimatter. We observe that most phenomena are $\mathcal{C}$- and $\mathcal{P}$-symmetric, and therefore, also $\mathcal{CP}$-symmetric. In particular, these symmetries are respected by the gravitational, electromagnetic, and strong interactions, but not by weak interaction. The situation changed in 1964, Christenson, Cronin, Fitch and Turlay were studying eigenstates of two neutral K mesons in the kaon decays, called short-lived and long-lived kaons, K_S^0 and K_L^0. If $\mathcal{CP}$ is conserved, the final states can be only $K_S^0 \to 2\pi$ and $K_L^0 \to 3\pi$ and mass eigenstates are also $\mathcal{CP}$ eigenstates. However, K_L^0 also sometimes decays to 2 pions, which implicates the $\mathcal{CP}$ eigenstates are different from the mass eigenstates and the K^0 and $\bar{K}^0$ can oscillate into each other, thus the $\mathcal{CP}$ symmetry is violated in certain rare processes.
There are three ways, how the $\mathcal{CP}$ can be violated in the Standard Model hadrons - $\mathcal{CP}$ violation in decay, in mixing and in the interference of mixing and decay.

The $\mathcal{CP}$ violation in decay (also know as direct $\mathcal{CP}$ violation) is the only possible source of $\mathcal{CP}$ asymmetry in charged meson decays. The decay amplitude of particle M into final state f is different from the decay amplitude of antiparticle into final anti-state,

$$\Gamma\left(M \to f\right) \neq \Gamma\left(\bar{M} \to \bar{f}\right). \tag{1.10}$$

The $\mathcal{CP}$ violation in mixing (or indirect $\mathcal{CP}$ violation) arises when the probability of oscillation from meson to anti-meson is different from the probability of oscillation from anti-meson to meson,

$$\text{Prob}\left(P^0 \to \bar{P}^0\right) \neq \text{Prob}\left(\bar{P}^0 \to P^0\right) \tag{1.11}$$

Thus the mass eigenstates are not $\mathcal{CP}$ eigenstates.

The $\mathcal{CP}$ violation in interference of mixing and decay occurs in case both meson and antimeson decay into the same final state, $M^0 \to f$ and $M^0 \to \bar{M}^0 \to f$. This case occurs for example in the decay of $B_s^0 \to J/\psi\phi$.

1.3 The CKM formalism

In 1963, Nicola Cabibbo[23] found, that the mass eigenstate and the interaction eigenstate of down and strange quark differ in the weak interaction. Nowadays, the masses and mixings of quarks have a common origin in the Standard Model. The Lagrangian for weak interactions of quarks can be expressed as [26]

$$\mathcal{L}_Y^q = -\frac{g}{\sqrt{2}} \bar{u_L}_i' \gamma^\mu 1_{ij} \bar{d_L}_j' W_\mu^+ + h.c., \tag{1.12}$$

where u_L' and d_L' are quarks fields denoting the interaction eigenvectors, γ^μ is Dirac matrix and W_μ^+ is gauge field. Writing interaction eigenvectors in term of mass eigenvectors

$d'_L = V^\dagger_{dL} d_L$ and $\bar{u}'_L = V_{uL} u_L$, the Lagrangian (1.12) is

$$\mathcal{L}^q_Y = -\frac{g}{\sqrt{2}} \bar{u_{Li}} \gamma^\mu \bar{V}_{ij} \bar{d_{Lj}} W^+_\mu + h.c., \tag{1.13}$$

where $V_{ij} = V^\dagger_{uL} V_{dL}$ is the CKM matrix (Cabibbo-Kobayashi-Maskawa matrix), denoted as

$$V_{CKM} = \begin{pmatrix} V_{ud} & V_{us} & V_{ub} \\ V_{cd} & V_{cs} & V_{cb} \\ V_{td} & V_{ts} & V_{tb} \end{pmatrix}. \tag{1.14}$$

1.3.1 PDG and Wolfenstein parametrisation

The matrix (1.14) is a complex 3×3 unitary matrix. Therefore it has 18 parameters (9 complex elements), however only four parameters are independent - 3 Euler mixing angles and one $\mathcal{CP}$-violating KM phase using the PDG parametrisation [1]. Defining $s_{ij} = \sin\theta_{ij}$, $c_{ij} = \cos\theta_{ij}$ and δ as phase causing $\mathcal{CP}$ violation, the CKM matrix (1.14) can be written as multiple of three matrices

$$V_{CKM} = \begin{pmatrix} 1 & 0 & 0 \\ 0 & c_{23} & s_{23} \\ 0 & -s_{23} & c_{23} \end{pmatrix} \begin{pmatrix} c_{13} & 0 & s_{13} e^{-\imath\delta} \\ 0 & 1 & 0 \\ -s_{13} e^{\imath\delta} & 0 & c_{13} \end{pmatrix} \begin{pmatrix} c_{12} & s_{12} & 0 \\ -s_{12} & c_{12} & 0 \\ 0 & 0 & 1 \end{pmatrix}, \tag{1.15}$$

each describing the two dimensional rotation. The angle θ_{12} is identified as Cabibbo angle. Wolfenstein [1] came with another parametrisation, which sets $s_{12} = \lambda$, $s_{23} = A\lambda^2$ and $s_{13} = A\lambda^3(\rho + \imath\eta)$. The CKM matrix is then

$$V_{CKM} = \begin{pmatrix} 1 - \lambda^2/2 & \lambda & A\lambda^3(\rho - \imath\eta) \\ -\lambda & 1 - \lambda^2/2 & A\lambda^2 \\ A\lambda^3(1 - \rho - \imath\eta) & -A\lambda^2 & 1 \end{pmatrix} + \mathcal{O}(\lambda^4). \tag{1.16}$$

However, this matrix is not in the unitary form. rewriting the matrix in terms $\bar{\rho} = \rho(1 - \lambda^2 + \cdots)$ and $\bar{\eta}$ makes the matrix unitary.

1.3.2 Unitary triangles

The unitarity condition of the CKM matrix can be more easily recovered by noting that $V_{CKM} V^\dagger_{CKM} = 1$ is equivalent to the orthogonality of columns or rows in V_{CKM} expressed as

$$\sum_{\alpha=u,c,t} V_{\alpha i} V^*_{\alpha j} = \delta_{ij}, \sum_{i=d,s,b} V_{\alpha i} V^*_{\beta i} = \delta_{\alpha\beta}. \tag{1.17}$$

The example of unitarity triangle is

$$V_{ud} V^*_{ub} + V_{cd} V^*_{cb} + V_{td} V^*_{tb} = 0, \tag{1.18}$$

which can be interpreted as triangles in the complex plane (see Fig. 1.2).

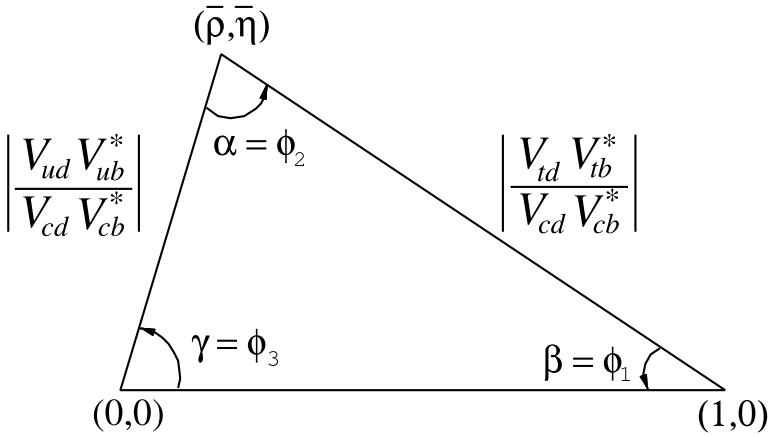

Figure 1.2: Unitarity triangle corresponding to the equation (1.18) [24].

This equation is often called B_d^0 triangle, because the angles α, β, γ from Fig. 1.2 are well measured in the B_d^0 decays. B_s^0 triangle gives the relation

$$V_{us}V_{ub}^* + V_{cs}V_{cb}^* + V_{ts}V_{tb}^* = 0, \tag{1.19}$$

from which the small angle

$$\beta_s = \arg\left(-\frac{V_{ts}V_{tb}^*}{V_{cs}V_{cb}^*}\right) \tag{1.20}$$

can be obtained. This angle is sensitive to $\mathcal{CP}$ violation via the element V_{ts} (at $\mathcal{O}(\lambda^4)$). Both B_d^0 and B_s^0 can be seen in Fig. 1.3.

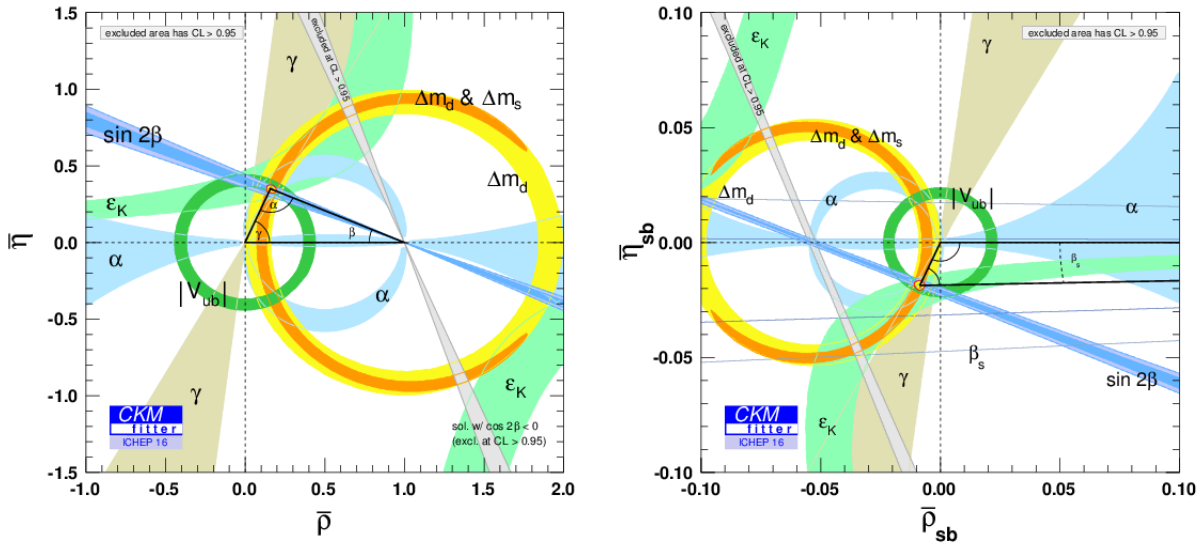

Figure 1.3: B_d^0 (left) and B_s^0 (right) triangles experimental results [25].

Chapter 2

B physics

2.1 B meson properties

The first experimental evidence of the b quark was observed in 1977 by Leon Lederman at Fermilab in proton beam collisions with fixed target made of copper and platinum. The Lederman's group observed resonance in the $m(\mu^+\mu^-)$ mass distribution around 9450 GeV. This narrow resonance was named Υ. It is an meson composed of one b quark and one b anti-quark. This meson has also heavier resonances, all together forming so called bottomonium (bounded state of the quark and anti-quark with same flavour, another example is charmonium $c\bar{c}$).
The B meson is combination of $q\bar{q}$ with nonzero beauty quantum number B and it is sometimes called open-beauty meson. Using this, the bottomonium (hidden-beauty, the beauty quantum number $B = 0$) is not considered B meson. The lowest mass B mesons are pseudoscalar particles, which can be charged or neutral. The summary of pseudoscalar B mesons is shown in the Tab. 2.1. Surprisingly, the B meson lifetime is larger than the lifetime of charmed mesons and its flight distance is ≈ 0.5 mm.

Name	Valence quark composition	Mass m [MeV]	Lifetime τ [ps]
$B^{\pm}$	$u\bar{b}$	5279.26 ± 0.17	1.519 ± 0.005
B^0_d	$d\bar{b}$	5279.58 ± 0.17	1.638 ± 0.004
B^0_s	$s\bar{b}$	5366.77 ± 0.24	1.512 ± 0.007
$B^{\pm}_c$	$c\bar{b}$	6275.6 ± 1.1	0.452 ± 0.033

Table 2.1: The lightest B mesons and their properties [1].

Usually, the beauty quark and its anti-quark are produced in pair. These quarks can be bound together forming the bottomonium or form hadron with another quarks in the collision. Then, Υ can decay into two B mesons, for example

$$\Upsilon\left(4^3S_1\right) \to B^0 + \bar{B}^0 \text{ or } B^+ + B^-. \tag{2.1}$$

Second possibility of producing b quark is the decay of the top quark into the final state containing the W boson and the b quark. This quark can then bind with another quark to form B meson. It is important to mention, that also top quarks and anti-quarks are formed in pairs. It means, that in most cases, also beauty quarks are formed in pair. This feature is used in many analyses in order to tag the charge of the B meson.
B mesons, due to their mass, decay weakly. The dominant decay mode of b quark in the B meson is $b \to c + W^-$ [1], where the W boson is virtual and decays into pair of leptons or quarks. The $b \to u + \cdots$ is also allowed, however it is suppressed by $|V_{ub}/V_{cb}|^2 \approx (0.1)^2$ relative to the $b \to c + \cdots$ [1]. Standard Model rare decays can also be observed, such as is the decay $B_s^0 \to \mu^+\mu^-$.
The study of the B mesons and their decays proved fruitful as it improved the understanding of hadronic processes. For example, semileptonic decays $B \to X_c l\nu$ and $B \to X_u l\nu$ are excellent way how to measure the magnitude of the CKM matrix elements V_{cb} and V_{ub}. Another example is measurement the $\mathcal{CP}$ violating phase $\phi_s = 2\beta_s$ from (1.20) in the mixing $B_s^0 - \bar{B}_s^0$.
Besides $\mathcal{CP}$ violation, there are many other fields of study - for example by measuring production cross-sections of beauty and charm hadrons and of the heavy flavour quarkonia, sensitive tests of QCD predictions of production in pp collisions could be provided.

2.2 $B_s - \bar{B}_s$ mixing in $B_s^0 \to J/\psi\phi$ decay

Neutral B mesons have the ability to oscillate from particle into its own antiparticle and back. As referred in the section 1.2.2 in the chapter 1, the flavour eigenstates are not equivalent to the mass eigenstates, the mixing is observed. The time evolution of the $B_s^0 - \bar{B}_s^0$ system can be described by the time dependent Schrödinger equation [26]

$$\imath\hbar\frac{\partial}{\partial t}\psi = \mathbf{H}\psi = \left(\mathbf{M} - \frac{\imath}{2}\mathbf{\Gamma}\right)\psi, \tag{2.2}$$

where ψ is the superposition of B_s^0 and $\bar{B}_s^0$, $\mathbf{M}$ is hermitian matrix providing mass terms and $\mathbf{\Gamma}$ is hermitian matrix describing the exponential decay

$$\mathbf{M} = \begin{pmatrix} M_{11} & M_{12} \\ M_{12}^* & M_{22} \end{pmatrix}, \ \mathbf{\Gamma} = \begin{pmatrix} \Gamma_{11} & \Gamma_{12} \\ \Gamma_{12}^* & \Gamma_{22} \end{pmatrix}. \tag{2.3}$$

Assuming the $\mathcal{CPT}$ symmetry is conserved, the diagonal terms $M_{11} = M_{22} = M$ and $\Gamma_{11} = \Gamma_{22} = \Gamma$ and the non-diagonal elements correspond to the $B_s^0 - \bar{B}_s^0$ mixing. If the $\mathcal{CP}$ symmetry is also conserved, the non-diagonal terms are equal, $M_{12} = M_{12}^*$ and $\Gamma_{12} = \Gamma_{12}^*$. The Schrödinger equation (2.2) can be solved by diagonalization of the matrix $\mathbf{H}$. The solution are two mass eigenstates with defined decay widths. These eigenstates are defined as B_H and B_L for the light and heavy state respectively,

$$\begin{aligned} |B_L\rangle &= p\left|B_s^0\right\rangle + q\left|B_s^0\right\rangle \\ |B_H\rangle &= p\left|B_s^0\right\rangle - q\left|B_s^0\right\rangle \end{aligned} \tag{2.4}$$

with complex coefficients p, q satisfying the normalisation condition $|p|^2 + |q|^2 = 1$.
Using the mass and lifetime of the eigenstates $|B_L\rangle$ and $|B_H\rangle$, the difference in mass and lifetime of the eigenvalues can be expressed as

$$\begin{aligned} \Delta m_s &= m_H - m_L \\ \Delta\Gamma_s &= \Gamma_L - \Gamma_H \\ M_s &= m_H + m_L \\ \Gamma_s &= \Gamma_L + \Gamma_H \end{aligned} \tag{2.5}$$

By definition Δm_s is positive, but $\Delta\Gamma_s$ can be negative. The Δm_s represents the mixing frequency of the $B_s^0 - \bar{B_s^0}$ oscillation.
Using equations (2.4) and (2.2), the mass eigenstates have a simple exponential evolution in proper time t,

$$\begin{aligned} |B_L(t)\rangle &= \exp\left(-\imath(M_L - \frac{\imath}{2}\Gamma_L)t\right)|B_L(0)\rangle \\ |B_H(t)\rangle &= \exp\left(-\imath(M_H - \frac{\imath}{2}\Gamma_H)t\right)|B_H(0)\rangle\,. \end{aligned} \tag{2.6}$$

The time evolution of flavour state B_s^0 and $\bar{B_s^0}$ can be obtained using this equation and (2.4),

$$\begin{aligned} \left|B_s^0(t)\right\rangle &= g_+(t)\left|B_s^0(0)\right\rangle + \frac{q}{p}g_-(t)\left|\bar{B_s^0}(0)\right\rangle \\ \left|\bar{B_s^0}(t)\right\rangle &= g_+(t)\left|\bar{B_s^0}(0)\right\rangle + \frac{p}{q}g_-(t)\left|B_s^0(0)\right\rangle, \end{aligned} \tag{2.7}$$

where

$$g_\pm(t) = \frac{1}{2}\mathrm{e}^{-\imath M_s t - \Gamma t/2}\left[\cosh\left(\frac{\Delta\Gamma_s}{2}t\right) \pm \cos\left(\Delta M_s t\right)\right]. \tag{2.8}$$

For simplification, the decay amplitudes at $t = 0$ can be denoted as

$$\begin{aligned} A_f &= \langle f|\,\mathbf{H}\left|B_s^0(0)\right\rangle \qquad \bar{A}_f = \langle f|\,\mathbf{H}\left|\bar{B_s^0}(0)\right\rangle \\ A_{\bar{f}} &= \left\langle \bar{f}\right|\mathbf{H}\left|B_s^0(0)\right\rangle \qquad \bar{A}_{\bar{f}} = \left\langle \bar{f}\right|\mathbf{H}\left|\bar{B_s^0}(0)\right\rangle. \end{aligned} \tag{2.9}$$

The differential decay rate is calculated by taking the modulus squared of the amplitudes (2.9). The branching ratio (decay rate) for $B_s^0 \to f$ can be expressed as [27]

$$\begin{aligned} \Gamma\left(B_s^0(t) \to f\right) =& \mathrm{e}^{\Gamma t}[\left(|A_f|^2 + |\frac{q}{p}\bar{A}_f|^2\right)\cosh\frac{\Delta\Gamma_s t}{2} + \left(|A_f|^2 - |\frac{q}{p}\bar{A}_f|^2\right)\cos\Delta M t \\ &+ 2\mathcal{R}e\left(\frac{q}{p}A_f^*\bar{A}_f\right)\sinh\frac{\Delta\Gamma_s t}{2} - 2\mathcal{I}m\left(\frac{q}{p}A_f^*\bar{A}_f\right)\sin\Delta M t]. \end{aligned} \tag{2.10}$$

The branching ratio for $\bar{B}_s^0$ looks similar:

$$\begin{aligned}\Gamma\left(B_s^0(t)\to f\right) =& \mathrm{e}^{\Gamma t}[\left(|A_f|^2+|\frac{q}{p}\bar{A}_f|^2\right)\cosh\frac{\Delta\Gamma_s t}{2}-\left(|A_f|^2-|\frac{q}{p}\bar{A}_f|^2\right)\cos\Delta M t \\ &+2\mathcal{R}e\left(\frac{q}{p}A_f^*\bar{A}_f\right)\sinh\frac{\Delta\Gamma_s t}{2}-2\mathcal{I}m\left(\frac{q}{p}A_f^*\bar{A}_f\right)\sin\Delta M t].\end{aligned} \tag{2.11}$$

In the most physics analyses, the branching ratio is usually expressed as the differential branching ratio using terms of the transversity formalisms [28]

$$\frac{\mathrm{d}^4\Gamma}{\mathrm{d}t\mathrm{d}\Omega}=\sum_{k=1}^{10}\mathcal{O}^k(t)g^k(\theta_T,\psi_T,\phi_T), \tag{2.12}$$

where $\mathcal{O}^k$ and g^k are functions described in Tab. 4 of the document [28]. Functions $\mathcal{O}^k$ contain the weak phase ϕ_s. The (2.12) is usually fitted from data with free parameters, where the most important are $\Delta\Gamma$, Γ_s and ϕ_s. However, fitting the function (2.12) is difficult. To improve the fit, the fit function is smeared by the Gauss function representing lifetime resolution or the angular acceptance is applied.

Opposite side tagging method

Another large impact on the measurement has method called flavour tagging. As it is written in the previous section, b mesons are produced in pair, so the initial flavour of neutral B-meson can be determined by the identification of the second hadron containing the second b quark. This method is called opposite side tagging method. To study and calibrate this other-side tagging, the decay of charged B meson can be used, because the charge is known by detecting the mesons daughter particle. The example of the calibration channel is $B^\pm\to J/\psi K^\pm$, where the charge of B meson is known and the opposite side is used for the identification when decaying into jets, muon or electron. The probability of correctly determined opposite charge is obtained.

2.2.1 Previous measurements

The measurement of the CP violation phase ϕ_s in the decay $B_s^0\to J/\psi\phi$ is carried out by several large experiments, the most important are LHCb, ATLAS and CMS at the LHC and D0 at Tevatron. Some of these detectors are optimized for B physics, so the results are considered precise. In the analyses, these experimental collaborations also use the information from the same side tagging (checking the charge and flavour composition of meson that comes from the same vertex as B_s^0) to improve the measurement.

D0 detector

D0 is the detector that has been operating at $p\bar{p}$ Tevatron collider. The data sample corresponds to an integrated luminosity of 8.0 fb^{-1} accumulated with the D0 detector

using $p\bar{p}$ collisions at $\sqrt{s} = 1.96$ TeV [29]. The oscillation frequency has been constrained to $\Delta m_s = (17.77 \pm 0.12)$ ps^{-1}. Including the systematic uncertainties, the phase ϕ_s and decay width difference are

$$\Delta\Gamma_s = 0.163^{+0.065}_{-0.064}\ \text{ps}^{-1} \qquad \phi_s = -0.55^{+0.38}_{-0.36}. \tag{2.13}$$

The 68%, 90% and 95% CL contours in the $\phi_s - \Delta\Gamma_s$ plane are in Fig. 2.1.

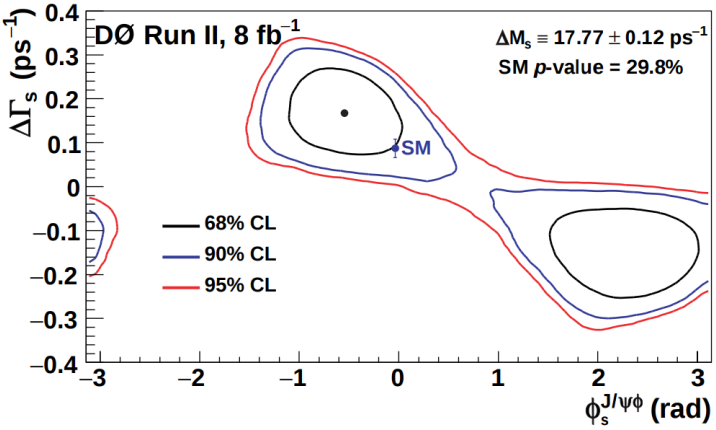

Figure 2.1: Likelihood confidence regions including systematic uncertainties measured at D0. The standard model expectation is indicated as a point with an error [29].

LHCb

The LHCb is the detector built exclusively for study of B physics. A sample of about 8500 $B_s^0 \to J/\psi\phi$ events isolated from 0.37 fb^{-1} of pp collisions at $\sqrt{s} = 7$ TeV was used in [30]. Due to the high fraction of tagged events in the signal sample $\epsilon = (24.9 \pm 0.5)\%$, an

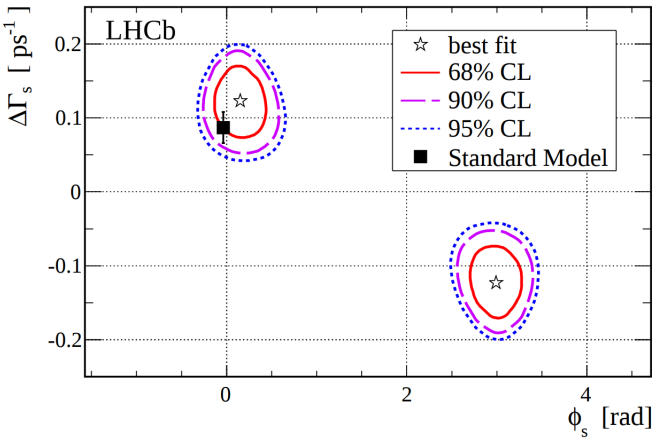

Figure 2.2: Likelihood confidence regions including systematic uncertainties measured at LHCb. The standard model expectation is indicated as a point with an error [30].

effective tagging efficiency is $TP = (1.91 \pm 0.23)\%$, so the tagging has large impact. The decay width difference $\Delta\Gamma_s$, the average decay width Γ_s and the phase ϕ_s are

$$\begin{aligned} \Gamma_s &= (0.657 \pm 0.009 \pm 0.008)\ \text{ps}^{-1} \\ \Gamma_s &= (0.125 \pm 0.029 \pm 0.01)\ \text{ps}^{-1} \\ \phi_s &= (0.15 \pm 0.18 \pm 0.06) \end{aligned} \tag{2.14}$$

and the 68%, 90% and 95% CL contours in the $\phi_s - \Delta\Gamma_s$ plane are shown in Fig. 2.2.

ATLAS

ATLAS is a general-purpose detector. It has been built to serve the purpose of allowing study the high p_{T} particle physics beyond the Standard Model (ATLAS was built to discover the basic block of matter, to investigate properties of the previously undiscovered Higgs boson). *pp* collisions data recorded at ATLAS can be also used for study of the CP violation in $B_s^0 - \bar{B}_s^0$ mixing. ATLAS B physics group measured the B_s^0 decay parameters using an integrated luminosity of 14.3 fb^{-1} collected by the ATLAS detector at $\sqrt{s} = 8$ TeV *pp* collisions at the LHC and combined them with earlier data using integrated luminosity 4.9 fb^{-1} and c.m.s. energy of $\sqrt{s} = 7$ TeV [28]. The opposite side tagging was used as well as at the LHCb experiment. However, the effective tagging efficiency of muon is smaller, $TP = (1.49 \pm 0.02)\%$. Using results of the full simultaneous unbinned maximum-likelihood fit of data at $\sqrt{s} = 8$ TeV and combining them with data at $\sqrt{s} = 7$ TeV, the decay width difference $\Delta\Gamma_s$, the average decay width Γ_s and the phase ϕ_s are

$$\begin{aligned} \Gamma_s &= (0.675 \pm 0.003 \pm 0.003)\ \text{ps}^{-1} \\ \Gamma_s &= (0.085 \pm 0.011 \pm 0.007)\ \text{ps}^{-1} \\ \phi_s &= (-0.090 \pm 0.078 \pm 0.041) \end{aligned} \tag{2.15}$$

and the 68%, 90% and 95% CL contours in the $\phi_s - \Delta\Gamma_s$ plane are shown in Fig. 2.3.

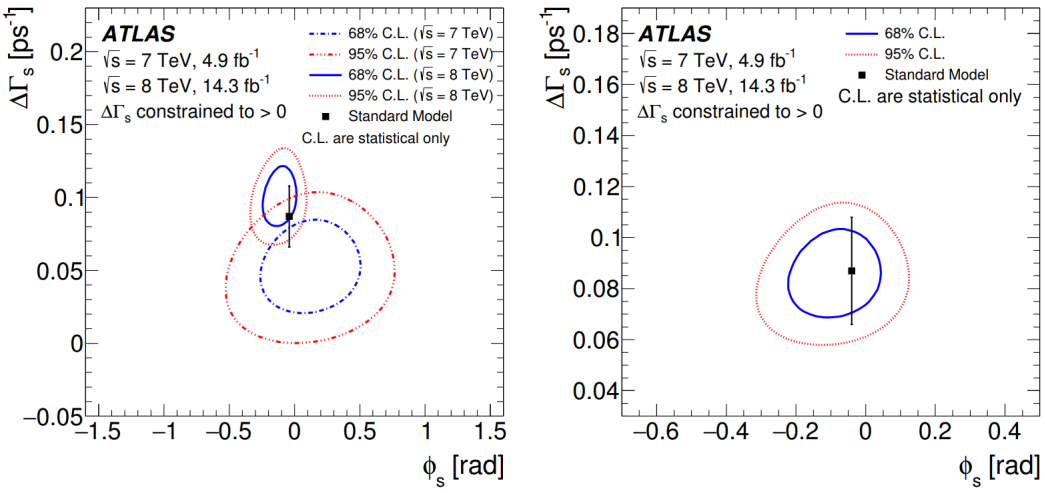

Figure 2.3: Likelihood contours in the $\phi_s - \Delta\Gamma_s$ plane for individual results from 7 TeV and 8 TeV data (left) and a final statistical combination of the results from 7 TeV and 8 TeV data (right). The standard model expectation is indicated as point with an error [28].

Chapter 3

The ATLAS Trigger System and Offline Software

3.1 The Trigger and Data Acquisition System

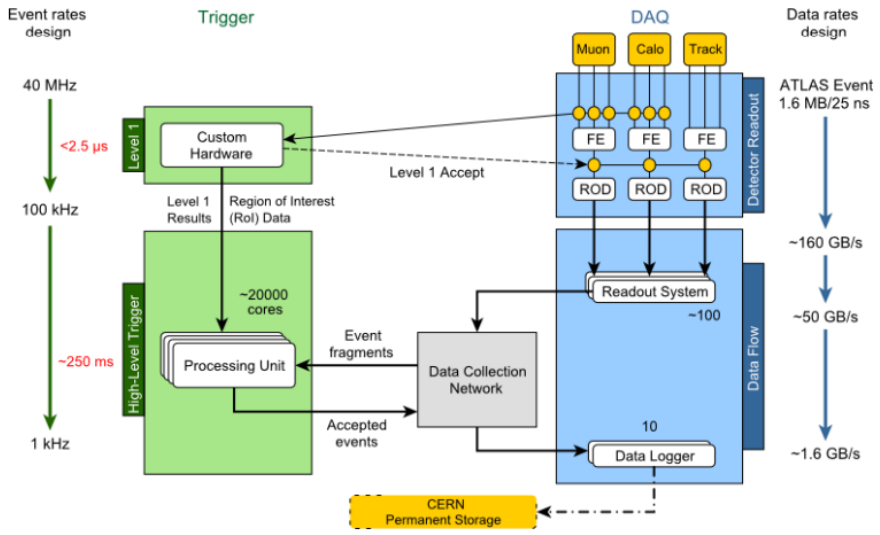

Figure 3.1: The architecture ATLAS Trigger and Data Acquisition System (TDAQ) in Run 2 [31].

The construction of the ATLAS detector at the LHC is described in [32]. Operating at the designed luminosity of 10^{34} cm^{-2}s^{-1}, the proton-proton bunch crossing designed frequency is 40 MHz [32]. In every bunch crossing dozens of protons interact, so the total interaction rate is approximately 1 GHz. Due to the technical limitations, only the event rate of about 1 kHz (in Run 2) can be recorded to tape. Therefore, it is important to select events with maximum efficiency in the selected physics channels. This reduction is performed by the Trigger System, which has two distinct levels, L1 and High-Level Trigger (merged L2 and

Event Filter for Run 1) [33]. The ATLAS Trigger and Data Acquisition System (TDAQ) in Run 2 is shown in Figure 3.1.
In the first stage of the ATLAS Trigger System, the L1 Trigger reduces the rate from 40 MHz to 100 kHz. Its decision is formed by the Central Trigger Processor (CTP), which uses information from Muon Spectrometer subdetectors and from all calorimeter subsystems. The L1 Calorimeter Trigger (L1Calo) searches events with high transverse energy E_T such as electron, photons, jets and τ-leptons decaying into hadron and also events with large total transverse energy and large missing transverse energy $E_{\mathrm{T}}^{\mathrm{miss}}$. The L1 Muon Trigger receives the signals from the muon trigger chambers RPC and TGC. It selects events with high-p_{T} muons based on six p_{T} thresholds, where muons are not counted in more than one threshold region.
The L1 Trigger latency is required to be less than 2.5 μs. The decision together with other signals is sent to the detector front-end system by the Timing, Trigger and Control system (TTC). In case the L1 Trigger accepts the event, the information is sent as Region-of-Interest (RoI) to the High-Level Trigger.
High-Level Trigger (HLT) works with additional detector information such as the Inner Detector hits, full information from Calorimeter and from muon detectors. The L2 Trigger inside the HLT reconstructs the track in RoI using fast reconstruction algorithms. When the event passes the L2 Trigger, the Event Filter will classify the selected event and reconstruct the event with complete detector information. The events are stored for offline reconstruction as 'RAW' data and the rate of recording of these events is 1 kHz. The information flow in the beginning with the rate of $\sim$ 10 PB/s is reduced to $\sim$ 1 GB/s. RAW data are further converted in the Athena framework into the xAOD data format, which is used for further physics analysis.

3.2 Muon reconstruction

The muons are an important tool for studying the variety of physical processes, including the B-physics and the study of charmonia, because charmonia can decay via the electromagnetic interaction into two oppositely charged muons. While events with these muons are triggered and saved to disk, they are reconstructed using information from the Inner Detector and Muon Spectrometer. Muon track candidates are connected with hits in segments of the detector (especially in the Muon Spectrometer). If the fit used for the hit association satisfies the selection criteria, the track is assigned to muon. There are four types of muons according to the muon reconstruction: Combined, Segment-tagged, Calorimeter-tagged and Extrapolated muons [34].

Combined muons: The reconstruction uses the fitted hits obtained independently by the Inner Detector and Muon Spectrometer. To improve the fit quality, some tracks can be added or removed. This refit can be made for example by the *STACO* or *MuId* algorithm [35]. These muons are used for the J/ψ reconstruction in order to ensure a good quality of the signal.

Segment-tagged muons: When the muon track crosses just one layer of the Muon Spectrometer due to the small p_{T}, these muons are used. The tracks in the Inner Detector are assigned to muons and extrapolated to the hit in the Muon Spectrometer. The common algorithm for these muons is *MuTag* [36].

Calorimeter-tagged muons: They are lowest purity muons are tracks in the Inner Detector associated with muons and the energy deposited in the Calorimeter but not connected with hits in the Muon Spectrometer. It is located primarily in the region, where is no Muon Spectrometer coverage because of the support system of the Inner Detector and the calorimeter [35].

Extrapolated muons: These muons, also called stand-alone muons, are associated only with the track in the Muon Spectrometer, which are extrapolated to the interaction point. To be classified as this type, the muon has to hit at least two layers of the Spectrometer. The track can be reconstructed for example by the *Muonboy* algorithm [36].

Detected particles can be also split into groups according their quality, tight, medium, loose and very loose [37].

Loose muons: The loose identification criteria are designed to maximize the reconstruction efficiency while providing good quality muon tracks. All muon types are used, calorimeter-tagged and segment-tagged muons are restricted to the area with psedorapidity $\eta \approx 0$ because of the cable in the area [37].

Medium muons: The Medium identification criteria provide the default selection for muons in ATLAS. They minimize the systematic uncertainties associated with muon reconstruction and calibration. Only combined and standalone muons are used in this selection. Standalone medium muons require at least three hits in each of the three layers of MDT or CSC. Combined medium muons satisfy condition of at least two hits on at least two layers of MDT [37].

Tight muons: Tight muons are selected to optimize the purity of the sample. Only CB tracks satisfying the Medium requirements are considered. To remove fake tracks,cuts on the the normalized chi-squared of the combined track fit and on the compatibility between the momenta measured in the ID and MS are applied [37].

Very loose muons: Hadrons sometimes can be mis-identified as muons. To suppress this contamination of muons, very loose selection is used.

3.3 ATLAS Offline Software

3.3.1 The Athena framework

A majority of the ATLAS software is implemented within the Athena, an object-oriented framework designed to provide a common infrastructure and environment for simulation, reconstruction and analysis applications of a high-energy physics experiment. It is based on C++ and Python and it is an implementation of the underlying Gaudi [38], architecture developed by the LHCb but commonly used by both ATLAS and LHCb.
The Athena is designed to provide an environment for simulation, filtering, reconstruction and analysis applications. It contains a skeleton of an application, into which the developers can plug-in their codes. Also in the Athena, the data in RAW format is transformed into xAOD (formerly AOD) and it serves as a central software repository of all algorithms.

3.3.2 ROOT framework

ROOT [40] is an object-oriented framework and it was originally designed at CERN by René Brun and Fons Rademakers. It has a C/C++ interpreter (CINT) and C/C++ compiler (ACLIC) and can be used as an interactive environment (running code in the command line) or execute scripts. Its large advantage is the ability to handle large files. It is able to make multi-dimensional histograms, curve fitting and storage of analysis results as ROOT files. ROOT provides the Virtual Monte Carlo interface to simulation engines such as Geant 4 and can be also used to develop an event display, an application providing the detector geometry or the particle path visualisation.
ROOT consists of about 3000 classes which contain the low-level building blocks of ROOT. The example of the class is *TFile*, *TObject* or *TClass*. The container classes provide the data structure classes like lists, maps, vectors and others and the trees and N-tuples can be made with the *TTree* and Ntuple classes [39]. The ROOT version 6.04.00 is primarily used to plot histograms in my analysis.

Roofit

Roofit [41] is a library of C++ classes providing the data fitting and modelling in the ROOT framework. In was originally developed for the BaBar collaboration at Stanford Linear Accelerator Center.
Roofit works with the normalised PDFs (Probability Density Functions) describing the probability density of the observables distribution with respect on the parameters of the density function. For example, the Gaussian density function with its parameter is

$$G(x,\mu,\sigma) = \frac{1}{A}\exp\left(-\frac{1}{2}\left(\frac{x-\mu}{\sigma}\right)^2\right), \qquad A = \int_{x_b}^{x_t}\exp\left(-\frac{1}{2}\left(\frac{x-\mu}{\sigma}\right)^2\right)\mathrm{d}x, \tag{3.1}$$

where x is the variable and μ, σ are parameters. If the limits of the integral are maximal and minimal, the integral is due to the normalisation equal to one.

Roofit can be used to perform unbinned and binned maximum likelyhood fits and produce plots. It also allows the multidimensional fitting, description of correlations between observables and the universal implementation of toy Monte Carlo sampling techniques.
The Roofit is used for fitting and computing fit parameters in my analysis.

sPlot

The sPlot [42] technique is a statistical tool dedicated to the analysis of a data sample consisting several sources of events (like signal and background source). These sources are merged into one sample which contains variables with known signal and background distributions. These variables are called discriminating variables. Using known distributions, sPlot can compute a particular weight (likeliness that the event is of signal type or background type). These weights (called sWeights) are applied on control variables, in order to obtain signal and background distributions separately. More details can be found in .
In this analysis, the B^+ mass is used as the discriminating variable and the muon charge is used as the control variable.

Chapter 4

Data analysis

4.1 Flavour tagging

B meson are produced at LHC during the hadronization of the $b\bar{b}$ pair. One b quark (it is unknown, whether it is quark or antiquark) is used to form the B_s^0 and second one from the pair is used for the identification when decaying into jets, muon or electron. This method is referred to as opposite-side tagging (OST). To study and calibrate this other-side tagging, the decay $B^{\pm} \to J/\psi K^{\pm}$ is used since the charge of the B-meson at production is provided by the kaon charge. It is expected, that detected particle on the opposite side of $B^{\pm}$ (usually muon, electron or jet) has opposite sign of charge to that which the detected kaon has. However leptons produced from cascade decays, $b \to c \to \mu$, will have the opposite charge and so the tag will be incorrect.
The tagging of flavour is achieved on a analysis basis, the quality of the tag value is measured. This quality is measured in terms of tagging efficiency, dilution, wrong tag fraction and tagging power.

Tagging efficiency

The tagging efficiency is the ratio of the events that can be used for tagging over the total number of events [28],

$$\epsilon_{tag} = \frac{N_r + N_w}{N_B}, \tag{4.1}$$

where N_r and N_w are number of correctly and incorrectly tag events and N_B is the total number of events with measured B meson.

Dilution and wrong tag fraction

The dilution describes the purity of the tagging,

$$D_{tag} = \frac{N_r - N_w}{N_r + N_w} = 1 - 2w_{tag}, \tag{4.2}$$

where the variable w_{tag} is the wrong tag fraction, the fraction of the incorrectly tagged events

$$w_{tag} = \frac{N_w}{N_r + N_w}. \tag{4.3}$$

Better tagging has the wrong tag fraction small (ideally zero) and the dilution close to 1.

Tagging power

Combining the efficiency and dilution, the tagging power is

$$P_{tag} = \epsilon D^2 = \sum_i \epsilon_i D_i^2. \tag{4.4}$$

The tagging power is not directly used as the calibration to $B_s^0 \to J/\psi\phi$ data, but it is useful when selecting the optimum tagging criteria and helps understanding of the tagging method by describing both the purity of tagging and the ratio of tagged events.

Cone charge and the tagging probability

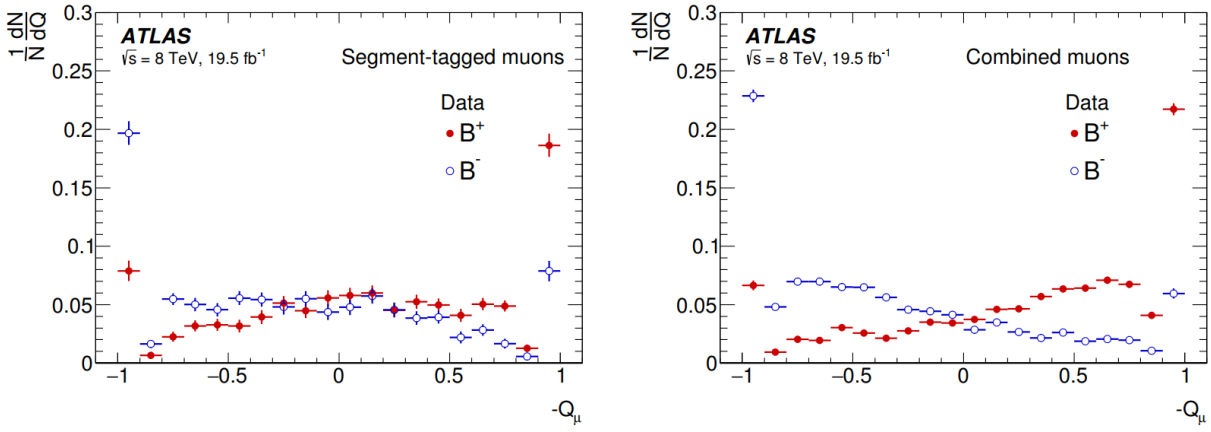

Figure 4.1: The opposite side cone charge distribution for $B^{\pm}$ candidates using the combined and segment tagged muons [28].

As written above, the opposite side b quark can decay as chain semileptonic decay $b \to c \to \mu$ instead of $b \to \mu$. To optimize the tagging performance, a cone charge variable is constructed around the muon, electron or jet, defined (for muons) as [28]

$$Q_\mu = \frac{\sum_i^{Ntracks} q_i \, (p_{\mathrm{T}})^\kappa}{\sum_i^{Ntracks} (p_{\mathrm{T}})^\kappa}, \tag{4.5}$$

where q_i is charge of the track, $\kappa = 1.1$ and the sum is performed over the reconstructed Inner Detector tracks within a cone $\Delta R = \sqrt{(\Delta\phi)^2 + (\Delta\eta)^2} < 0.5$ around the muon

direction[1]. The cone charge distribution is in Figure 4.1. If there are no additional tracks within the cone, the charge of the muon is used. Tracks associated with $B^{\pm}$ are excluded from the cone charge. The cone charge for combined and segment tagged muons can be seen in Fig. 4.1.
To transfer the information about tagging from $B^{\pm}$ into B_s^0 events, the tagging probability is used. Probability, that specific event has decay containing b quark (B^- meson) or $\bar{b}$ (B^+ meson) is denoted as $P(Q|B^+)$ or $P(Q|B^-)$, respectively. Then, the probability to tag the event as containing $\bar{b}$ is [28]

$$P(B|Q) = \frac{P(Q|B^+)}{P(Q|B^+) + P(Q|B^-)} \tag{4.6}$$

and $P(\bar{B}|Q) = 1 - P(B|Q)$ is probability to tag the event as containing b. The probability distribution for segment tagged muons, separated into single-track events (left) and cone-charge (right) are in Fig. 4.2.

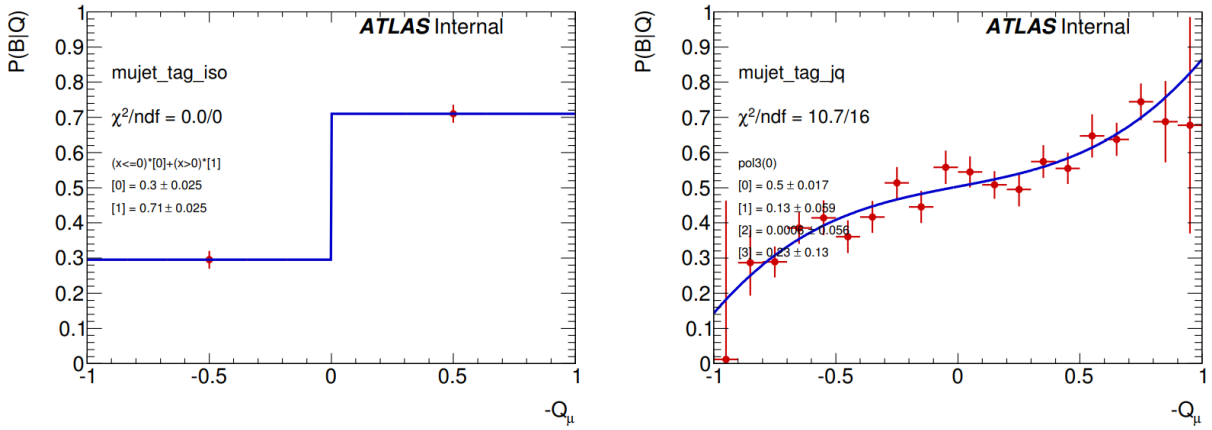

Figure 4.2: The probability distribution for segment tagged muons, separated into single-track events (left) and cone-charge (right) [28].

4.2 Data selection

The data used in this analysis were taken by the ATLAS experiment at the LHC in proton-proton collisions during the year 2016 with energy $\sqrt{s} = 13$ TeV. The Good Runs List All Good/data16_13TeV. periodAllYear_HEAD_DQDefects-00-02-04_PHYS_StandardGRL_All_Good.xml has been applied at the Athena level to remove the luminosity blocks that are not good to be used for physics analysis. The B candidate must satisfy mass condition $5.0 < m(B) < 5.7$ GeV and pseudorapidity $|\eta(B)| < 2.5$. Additionally, candidates must pass the lifetime cut $\tau > 0.2$ ps applied to remove prompt component of background

[1]The pseudorapidity detector coordinate is defined as $\eta = -\ln\tan(\Theta)$, where Θ is the polar angle from the beam axis. ϕ is the azimuthal angle around the beam axis.

and the probability of the vertex fit must be better than $\chi^2 < 10.8$ for one degree of freedom. Additionally, the kaon must satisfy $p_{\mathrm{T}}(K) > 1$ GeV and $|\eta(K)| < 2.5$ and the J/ψ candidates are made of two oppositely-charged muons with transversal momentum $p_{\mathrm{T}}(\mu) > 4$ GeV and pseudorapidity within $|\eta(\mu)| < 2.5$. The third muon used for opposite tagging passes the $|\eta(\mu)| < 2.5$ and $p_{\mathrm{T}}(\mu) > 2.5$ GeV criteria.

4.3 $B^{\pm} \to J/\psi K^{\pm}$ mass fit

4.3.1 Fit model

An unbinned maximum likelihood fit is performed using roofit on the selected data to fit the invariant mass of B^+ and B^- in the exclusive channel. The signal part is described by two Gauss functions with the same mean. The background is defined by combination of exponential constant function to describe the overall background and by inverse hyperbolic tangent function to describe partially reconstructed B candidates. Then, the total likelihood function is defined as a combination of the signal and background probability

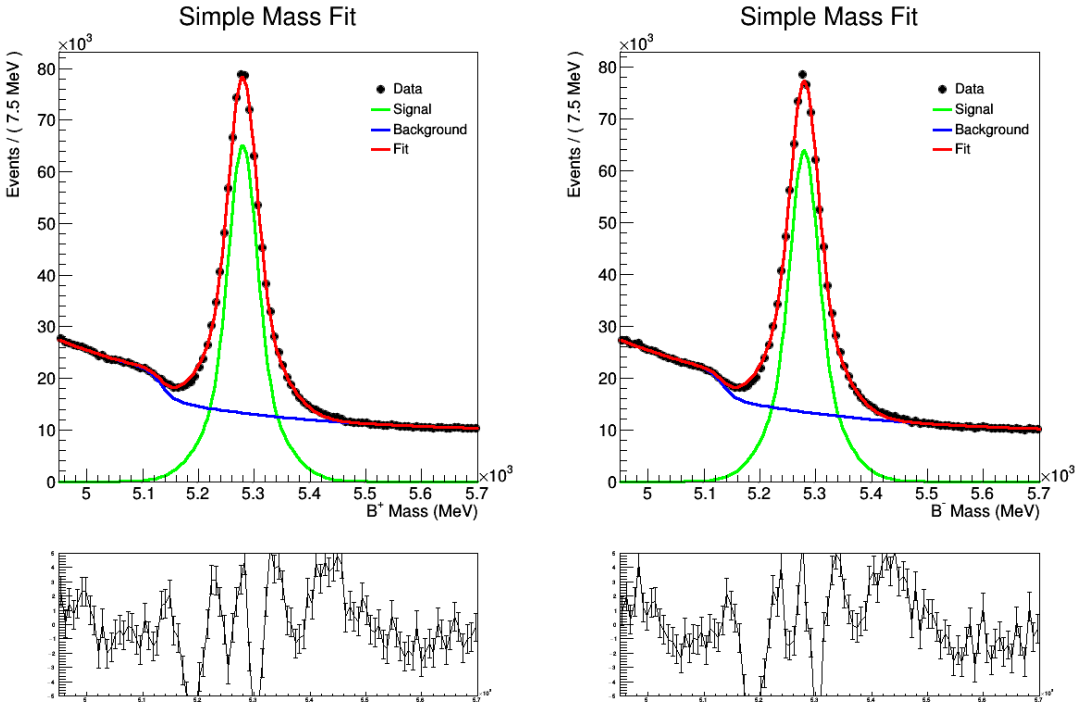

Figure 4.3: The invariant mass distribution of B^+ (left) and B^- (right) candidates that passed the selection criteria. The overall result of the fit is given by the red curve, the signal component is given by the green curve and the background function with the partially reconstructed B is given by the blue curve.

density functions

$$\begin{aligned}\text{PDF} =& f_{sig}[f_{gauss}G_1(\mu,\sigma_1) + (1-f_{gauss})G_2(\mu,\sigma_2)] + \\ &+ (1-f_{sig})[f_{bck1}E(\lambda) + f_{bck2}C + (1-f_{bck1}-f_{bck2})AT(sc,of)],\end{aligned} \tag{4.7}$$

where $G_1(\mu,\sigma_1)$ and $G_2(\mu,\sigma_2)$ are Gauss functions with the same mean μ, $E(\lambda)$ is the exponential function with the slope λ, C is constant function and $AT(sc,of)$ is atanh with the offset of and scale sc. The coefficients f_{sig}, f_{gauss}, f_{bck1} and f_{bck2} are the scale factors between the functions. The coefficients of the fit are in the Table 4.1 and the result plots are shown in the Figure 4.3.

	μ	σ_1	σ_2	λ	sc	of	f_{sig}	f_{gauss}	f_{bck1}	f_{bck2}
value	5279.38	24.5	58.8	-0.00360	-0.042	5133.9	0.331	0.506	0.282	0.627
uncertainty	0.06	0.2	0.5	0.00006	0.002	0.79	0.001	0.006	0.006	0.004
value	5279.45	23.9	56.5	-0.00340	-0.043	5133.4	0.325	0.481	0.311	0.605
uncertainty	0.06	0.2	0.5	0.00007	0.003	0.9	0.001	0.006	0.009	0.005

Table 4.1: Fitted parameters of the total probability density function (4.7). The constant function C is set to be free because of the fit function normalization. μ, σ_i are measured in MeV, meanwhile λ and sc are measured in MeV^{-1}. Rest of parameters is dimensionless.

4.3.2 Sideband subtraction

To study parameter distribution corresponding to the $B^{\pm}$ signal with the background subtracted, sPlot (described in the section 3.3.2) or sideband subtraction can be used.
It is assumed that the background distribution of quantity of interest under the signal peak is approximately identical to the distribution of the background away from the peak region.
There are three mass distribution regions defined. The signal region (histogram $H1$ in Figure 4.4) is defined to be $\pm 2\sigma$ around the Gauss mean, where σ is normalisation-weighted average sigma between the narrow and wide Gauss functions (for B^+ it is $\sigma = 44.8 \pm 0.3$, for B^- it is $\sigma = 44.0 \pm 0.3$). The left ($H2$ in Figure 4.4) and right ($H3$ in Figure 4.4) sideband region are the mass interval $(\mu - 5\sigma; \mu - 3\sigma)$ and $(\mu + 3\sigma; \mu + 5\sigma)$. Approximately 90% of the signal events are retained.
The parameter distribution mention in Fig. 4.4 can be also used for the opposite side tagging method. Defining histogram of the opposite side muons charge for $B^{\pm}$ candidates in mass signal region $G1$ and histograms of the opposite side muons charge for $B^{\pm}$ candidates in left and right sideband regions $G2$ and $G3$, the number of charged third muons is

$$G_{final} = G1 - \frac{Nbg_{sigreg}}{Nbg_{LSB} + Nbg_{RSB}}\,(G2 + G3) = A\,(G2 + G3)\,, \tag{4.8}$$

where Nbg_{RSB}, Nbg_{LSB} and Nbg_{sigreg} are numbers of muons defined in the Figure 4.4 and their values with statistical errors for both B^+ and B^- are in Table.

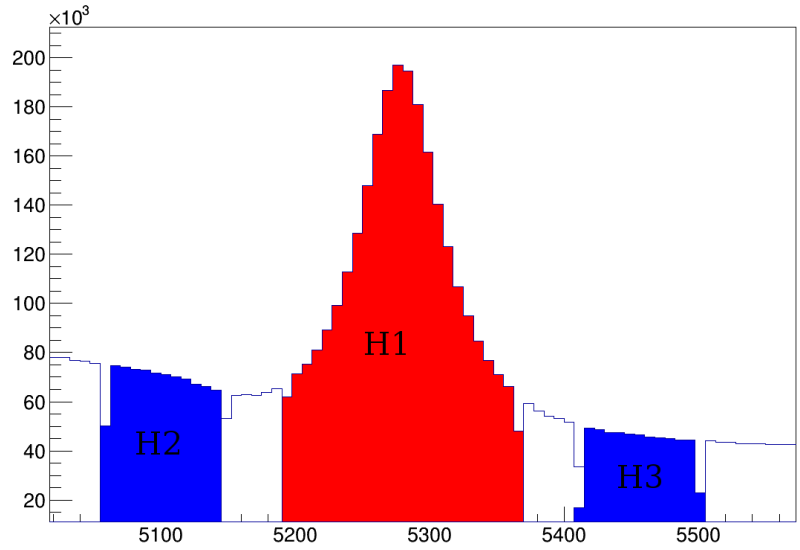

Figure 4.4: The sideband subtraction method. $H1$ is the signal region with the number of background candidates Nbg_{sigreg}, $H2$ and $H3$ are the sideband regions with the number of background candidates Nbg_{LSB} and Nbg_{RSB}.

	Nbg_{SIGREG}	Nbg_{LSB}	Nbg_{RSB}	A
B^+	319600 ± 500	256300 ± 400	137600 ± 200	0.812 ± 0.002
B^-	316300 ± 500	247200 ± 400	135000 ± 200	0.828 ± 0.002

Table 4.2: Values and errors of the parameters from the equation (4.8) and Figure 4.4.

4.4 Single muon tagging

The study of single muon tagging is still under the progress and it serves for informative purposes now, so the error (statistical and systematic) is not calculated in this section. Only place, that is used in the analysis, is the tag probability, which will be presented in section 4.6.

Order of selection criteria

There are two possibilities, how split muons into groups - by the muon quality or by the muon type (see section 3.2). The previous analysis has been made using the combined and segment-tagged muons and only one muon with highest transversal momentum (p_{T}) per event is selected. However, the classification of muons between Run-1 and Run-2 has changed, so both ways have to be tested. Moreover, the order of selection criteria is important. There are two possibilities of selection criteria order:

- In each event, muon with highest p_{T} is selected. Then, its type or quality is checked.

- Firstly, the quality or type of all muons in each event is checked. The group with only the best quality (tight muon has better quality than medium muon, medium muon has better quality than loose muon, etc.) is used. If there is no tight muon, the group with medium quality muons is used and so on. Then, muon with highest p_{T} in the selected group is only used for the tagging.

	$\epsilon_{\mathbf{tag}}$ (%)	$\mathbf{D_{tag}}$	$\mathbf{w_{tag}}$	$\mathbf{P_{tag}}$ (%)	$\epsilon_{\mathbf{tag}}$ (%)	$\mathbf{D_{tag}}$	$\mathbf{w_{tag}}$	$\mathbf{P_{tag}}$ (%)
tight	3.016	0.392	0.304	0.463	4.18	0.355	0.323	0.526
medium	0.158	0.143	0.429	0.003	0.21	0.114	0.443	0.003
loose	0.121	0.091	0.455	0.001	0.17	0.088	0.456	0.001
very loose	6.017	0.031	0.485	0.006	7.93	0.028	0.486	0.006

Table 4.3: The tag efficiency ϵ_{tag}, dilution D_{tag}, wrong tag fraction w_{tag} and tag power P_{tag} for different muon qualities. The left table shows results for order of selection criteria, where higher p_{T} has higher priority than muon quality. The right table shows results selection criteria, where muon quality has higher priority than higher p_{T}. Results serves for the informative purpose, so their errors has not been calculated yet. Tables are produced using the sPlot.

	$\epsilon_{\mathbf{tag}}$ (%)	$\mathbf{D_{tag}}$	$\mathbf{w_{tag}}$	$\mathbf{P_{tag}}$ (%)	$\epsilon_{\mathbf{tag}}$ (%)	$\mathbf{D_{tag}}$	$\mathbf{w_{tag}}$	$\mathbf{P_{tag}}$ (%)
combined	5.270	0.244	0.378	0.313	7.44	0.219	0.391	0.356
segmentTag	0.512	0.044	0.478	0.001	0.75	0.037	0.482	0.001
caloTag	3.531	0.026	0.487	0.002	4.30	0.021	0.490	0.002

Table 4.4: The tag efficiency ϵ_{tag}, dilution D_{tag}, wrong tag fraction w_{tag} and tag power P_{tag} for different muon types. The left table shows results for order of selection criteria, where higher p_{T} has higher priority than muon type. The right table shows results selection criteria, where muon type has higher priority than higher p_{T}. Results serves for the informative purpose, so their errors has not been calculated yet. Tables was produced using the sPlot.

To provide the necessary data test, only part of the 2016 statistics has been used. The results are in Tables 4.3 and 4.4. The stand alone muons are considered in both tables, but at the end of the selection chain, the are thrown away. This together with selection order cause lower total efficiency of the left table. The dilution seems to be similar in both selection chains and the tag power is higher for the second selection chain. Comparing the tag power with respect to the muon quality and muon type, the tight muon has considerable higher tag power. This leads to the conclusion to use only the tight muons for the tagging and exclude the standalone muons from the analysis. The main reason of exclusion of the standalone muons is due to its different definition in earlier version of ATLAS software, where standalone muons were in whole $p_{\mathrm{T}} - \eta$ region, instead of the expected $2.5 < |\eta| < 2.7$, see Figure 4.5.

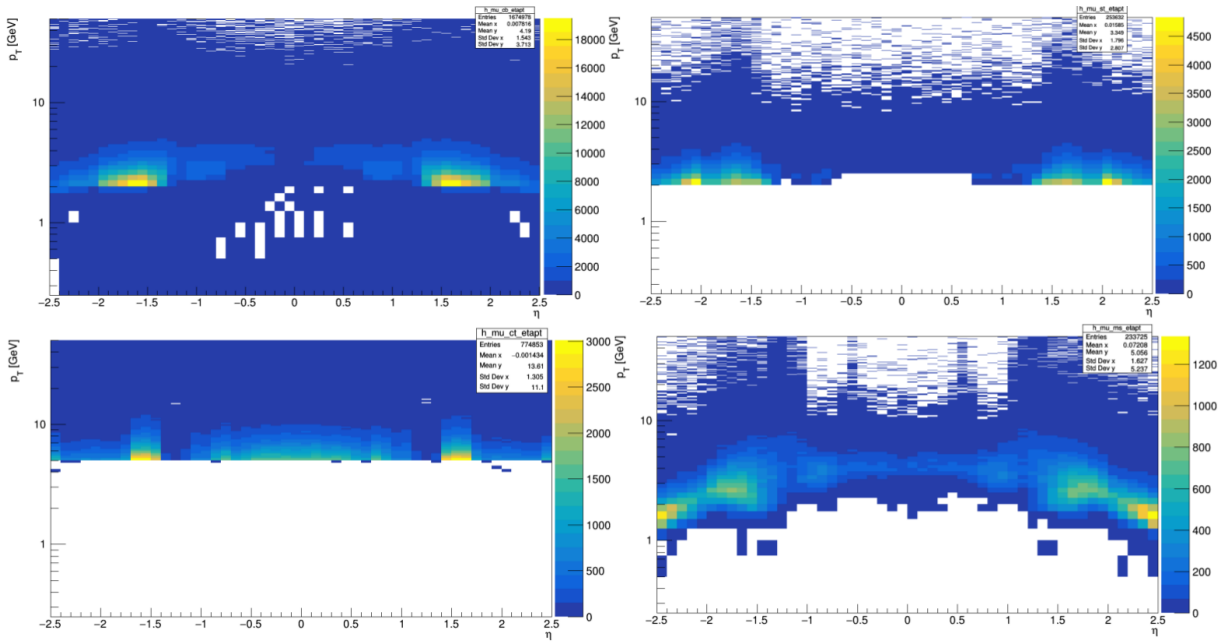

Figure 4.5: The $p_{\mathrm{T}} - \eta$ distribution for combined muons (left top), segment-tagged muons (right top), calo-tagged (left bottom) and standalone (right bottom). All third muons included (not those from decay of J/ψ).

Sideband subtraction versus sPlot

During the analysis, there were two options, how to calculate the tag power for muons - the sideband subtraction (described in previous section) and the sPlot (described in section 3.3.2). In order to compare these two methods, same statistical sample as for the Table 4.4 was used. The comparison is shown in the Table 4.5. The sideband subtraction method has slightly higher efficiency than in results of the sPlot method. Despite this fact, the tag power for both methods is similar, so both methods are equivalent. Because of the clarity of the code and fast data handling, only sPlot is used in later analysis.

	$\epsilon_{\mathbf{tag}}$ (%)	$\mathbf{D_{tag}}$	$\mathbf{w_{tag}}$	$\mathbf{P_{tag}}$ (%)	$\epsilon_{\mathbf{tag}}$ (%)	$\mathbf{D_{tag}}$	$\mathbf{w_{tag}}$	$\mathbf{P_{tag}}$ (%)
combined	7.44	0.219	0.391	0.356	7.88	0.215	0.393	0.366
segmentTag	0.75	0.037	0.482	0.001	0.80	0.030	0.484	0.001
caloTag	4.30	0.021	0.490	0.002	4.40	0.025	0.488	0.003

Table 4.5: The tag efficiency ϵ_{tag}, dilution D_{tag}, wrong tag fraction w_{tag} and tag power P_{tag} for different muon qualities. Left table contains results using the sPlot method, right table shows results obtained using the sideband subtraction method. Both tables use same selection criteria, where muon type has higher priority than higher p_{T}. Results serves for the informative purpose, so their errors has not been calculated yet.

Additional cuts

Solving the issue with tagging method, usage of type or quality criteria and the order of selection criteria, the tag power in Tables 4.4, 4.3 and 4.5 is still smaller that the tag power from the Run 1 analysis [28]. The reason can be larger pile-up[2] in Run-2.Therefore, some additional cuts had to be made. For example, muon should pass Δz cut of the primary vertex. As it is visible in Figure 4.6, the impact parameter of muon trajectory relative to primary vertex must be smaller than $|\Delta z| < 5$ mm.
Table 4.6 (left) shows final efficiency, dilution and tag power after applying the Δz cut. The whole 2016 statistics has been used to produce this table, including more track, that can be identified as decay in flight muons (from kaon or pions). This leads to higher efficiency of very loose muons.
The tag power for tight muons looks satisfactorily, it has higher value than the tag power from [28], where is was improved by the cone charge.

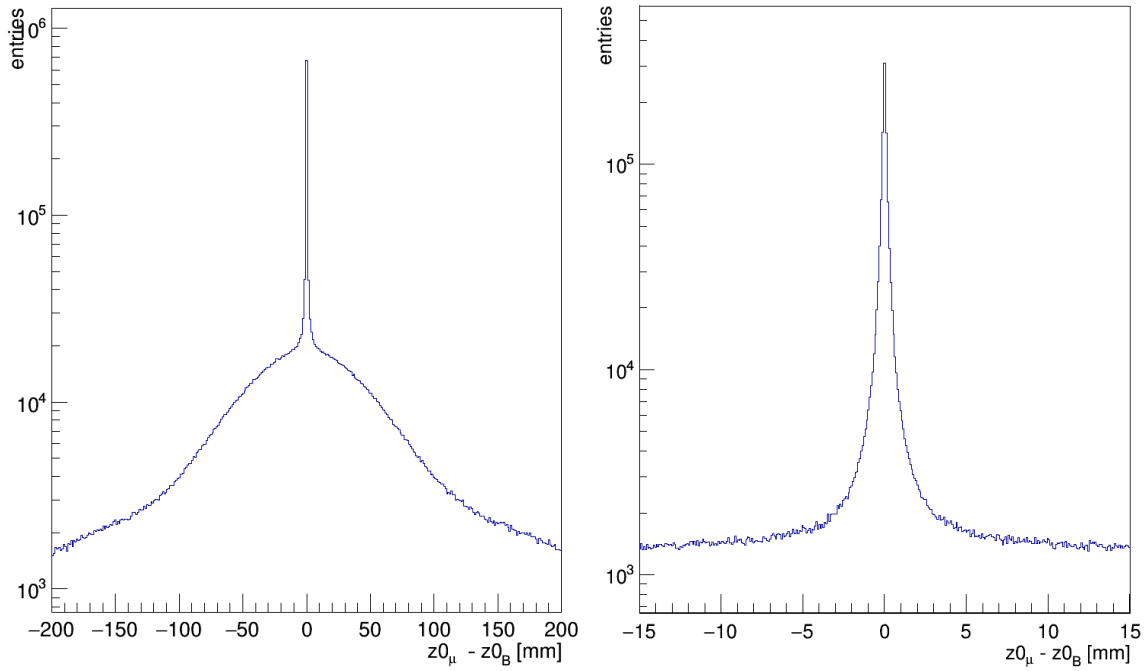

Figure 4.6: Left figure shows distribution of Δz, where Δz is impact parameter of muon trajectory relative to primary vertex identified in the event using B-signal candidate. The narrow peak represents signal muon candidates and the area under this peak represents the pile-up. Right figure is just the left one with magnification of the central part.

[2]The high luminosity of the LHC results in a significant background to interesting physics events known as pile-up, proton-proton collisions in addition to the collision of interest.

Release 20.7 versus 21

Within this analysis, the applicable ATLAS analysis software release has been upgraded from version 20.7 to version 21. In this upgrade, the reconstruction of RAW data has been improved. For this analysis, it means that muons should be reconstructed better and purer, avoiding the misidentification of kaons and pions as muons (decays in flight).
After muon reconstruction improvement, taking the whole 2016 statistics, similarly to results in left Table 4.6, the tag efficiency, dilution and power are in the right Table 4.6. Also the p_{T} dependence has been checked, see Figures 4.7, 4.8 and 4.9. Dilution appears to have plateau around 50% from $p_{\mathrm{T}} > 10$ GeV. Tight muons has still highest tag power, increasing after the software release changes up to 1.32%.

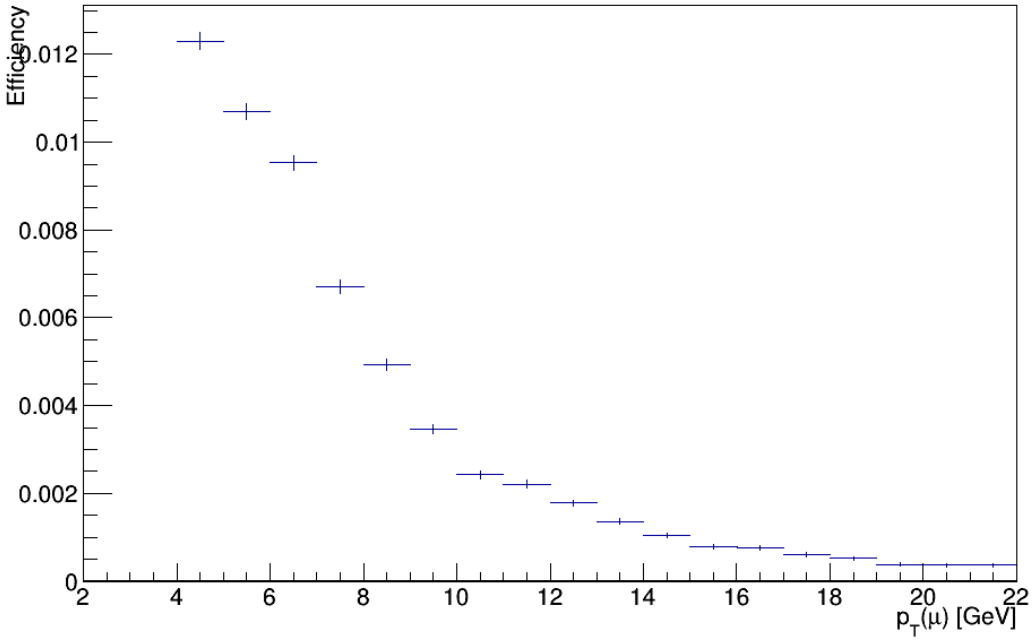

Figure 4.7: The muon transversal momentum dependence of the muon efficiency. The errors are statistical errors and they were calculated as the sum of the square of weights per bin.

	$\epsilon_{\mathbf{tag}}$ (%)	$\mathbf{D_{tag}}$	$\mathbf{w_{tag}}$	$\mathbf{P_{tag}}$ (%)	$\epsilon_{\mathbf{tag}}$ (%)	$\mathbf{D_{tag}}$	$\mathbf{w_{tag}}$	$\mathbf{P_{tag}}$ (%)
tight	7.75	0.358	0.32	0.996	6.50	0.451	0.275	1.32
medium	0.47	0.122	0.44	0.007	2.41	0.253	0.373	0.15
loose	0.35	0.093	0.45	0.003	0.98	0.175	0.413	0.03
very loose	12.52	0.044	0.48	0.024	17.7	0.062	0.469	0.07

Table 4.6: The tag efficiency ϵ_{tag}, dilution D_{tag}, wrong tag fraction w_{tag} and tag power P_{tag} for different muon qualities with applied Δz cut on all 2016 data, where other tracks were included (so the efficiency is higher - approximately twice). Results for release 20.7 (left) and release 21 (right).

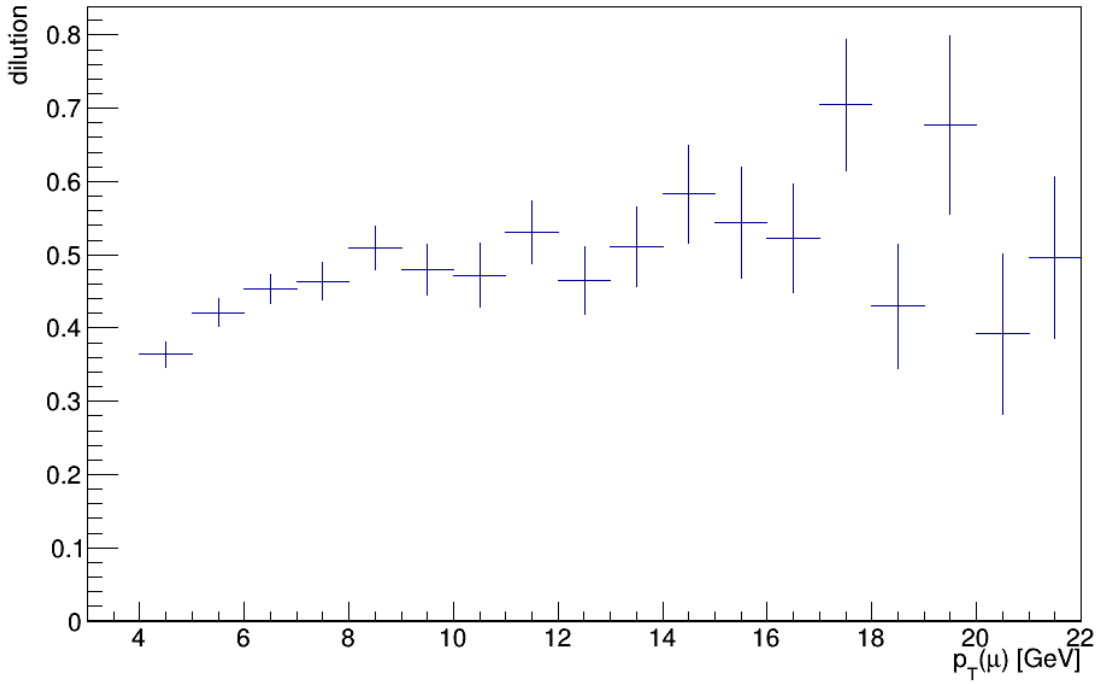

Figure 4.8: The muon transversal momentum dependence of the tag dilution. The errors are statistical errors and they were calculated as the sum of the square of weights per bin.

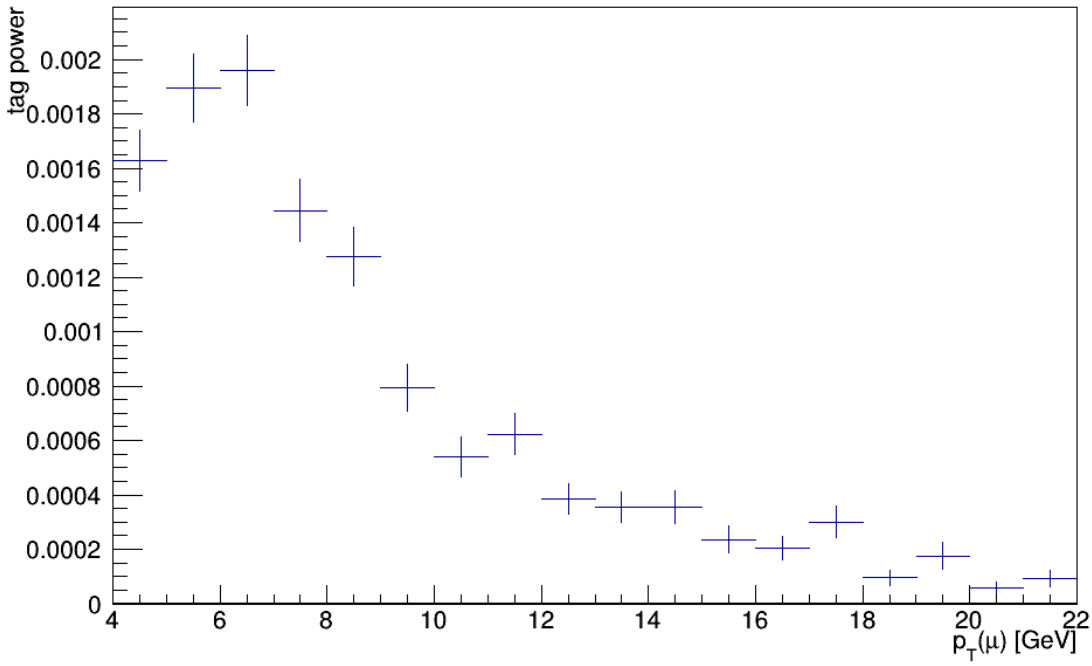

Figure 4.9: The muon transversal momentum dependence of the tag power. The errors are statistical errors and they were calculated as the sum of the square of weights per bin.

4.5 Cone charge tagging

The cone charge is used for optimization of the tagging performance and it can be defined by the equation (4.5). The cone $\Delta R = \sqrt{(\Delta\phi)^2 + (\Delta\eta)^2} < 0.5$ is constructed around selected muon. Only tight muons are used as the leading muon (all cuts are applied on this muon, including the Δz cut) and the tracks of B candidate (and its muons from J/ψ) and kaon are not included in the cone around these muons. No other cuts on track in cone are applied. Sometimes, there is no additional track in the cone around the muon. Then the cone charge has value of ± 1, see Figure 4.10
The tag power in the cone charge case is

$$P_{tag} = \sum_i (\epsilon_{tag})_i \left(2P_i(B^+|Q_i) - 1\right)^2, \tag{4.9}$$

where $P_i(B^+|Q_i)$ is the cone charge for B^+. The B^- tag power can be calculated in the same way and is equal to the B^+ tag power, so there is no need to do that.
Both ATLAS software releases 20.7 and 21 were tested. It is expected, that the results for the release 21 would have higher tag power, similarly to the results for the single muon tag power.

All qualities of muons

Firstly, the tag power for qualities of muons were calculated, see Table 4.7. It allows to omit the calculation of tag power for cones around medium, loose and very loose muons due to its small tag power. However, the tag power using the cone charge method has smaller tag power than the single muon has (see Table 4.6 left, where results for release version 20.7 are presented). This implies, that there are some polluting track in the cone, which decrease the tag power, or the coefficient κ is different than expected.

	tight	medium	loose	very loose
$P_{tag}(\%)$	0.984	0.020	0.026	0.038

Table 4.7: Tag power P_{tag} of cone charge for all qualities of leading muon. The cone charge method on data of release version 20.7 was used to obtain these results.

κ variation

The stability of cone charge with varying the power coefficient κ in (4.5) was also tested. In previous analysis, κ was set to be 1.1 (provided the highest tag power), so the κ variation test was made around this value. Results for both software releases can be seen in Table 4.8. For both releases, despite the fact there are some small deviations, the tag power for different κ seems to be stable and the value $\kappa = 1.1$ can be used. However, the tag power is still smaller for cone charge than for the single muon charge, so more investigation is needed.

κ	1.00	1.05	1.10	1.15	1.20
$P_{tag}(\%)$	0.975	0.986	0.984	0.981	0.987
$P_{tag}(\%)$	1.306	1.311	1.312	1.318	1.317

Table 4.8: Tag power P_{tag} for κ variation in (4.5). Results for release 20.7 results are shown on the first line, results for release 21 on the second one.

4.5.1 Δz and ΔR variation

Secondary particles created in collisions at the centre of the ATLAS detector pass through the layers. This passage can cause interaction of these particles with detector, creating another particles. Also particles created in B meson decay (J/ψ, kaons, muons, electrons) hit some layers of the detector. This can together with pile-up cause the pollution of the cone charge created around the muon.

ΔR	no cut	< 0.1	< 0.2	< 0.3	< 0.4	< 0.5
$P_{tag}(\%)$	0.984	1.056	1.138	1.207	1.236	1.247
$P_{tag}(\%)$	1.312	1.374	1.454	1.506	1.535	1.541

Table 4.9: The ΔR cut between B candidate and tracks in the muon cone. The $\Delta R < 0.2$ cut means that all tracks in the cone of $\Delta R < 0.2$ around the B candidate are excluded from the cone around the leading muon. Results for release 20.7 results are shown on the first line, results for release 21 on the second one.

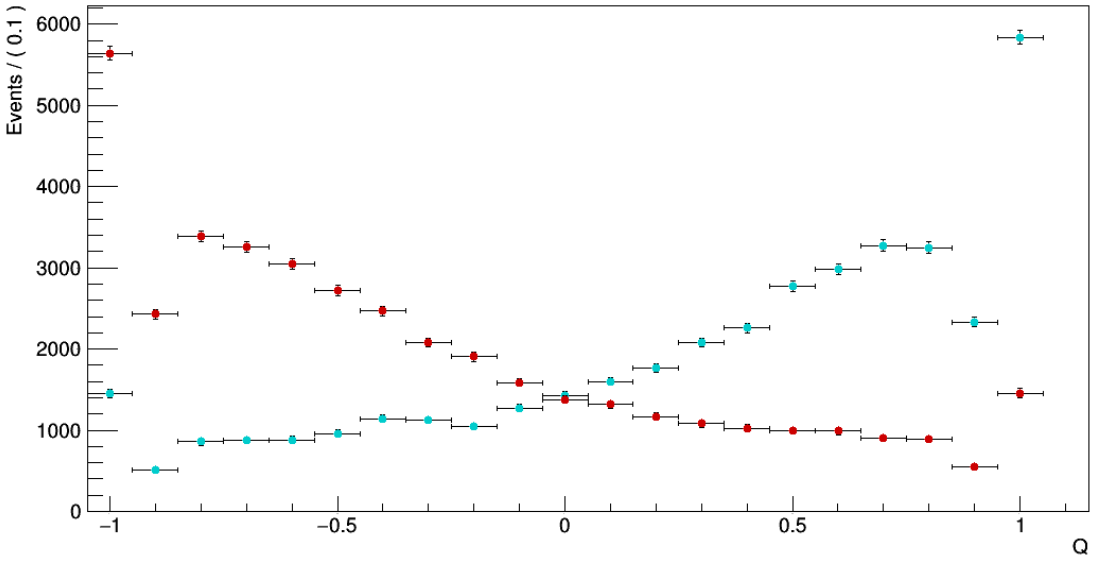

Figure 4.10: The muon cone charge distribution (red B^+, blue B^-) for $\Delta R < 0.4$ (all tracks in the cone of $\Delta R < 0.4$ around the B candidate are excluded from the cone around the leading muon).

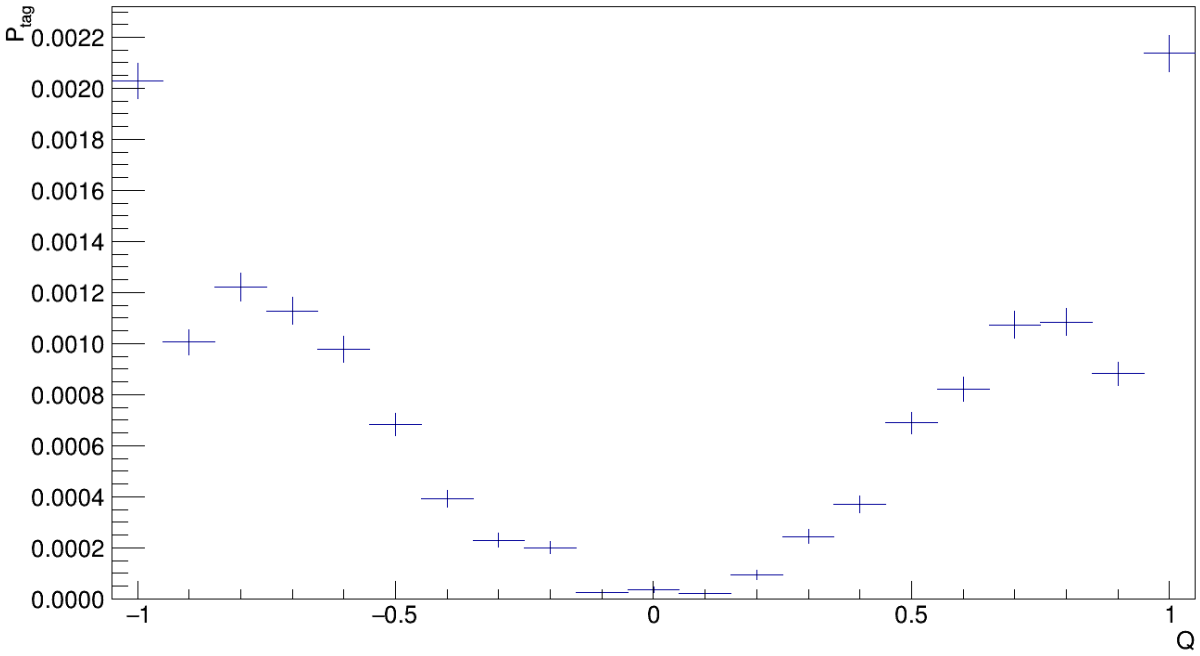

Figure 4.11: The tag power distribution with dependence on cone charge for $\Delta R < 0.4$ (all tracks in the cone of $\Delta R < 0.4$ around the B candidate are excluded from the cone around the leading muon).

To reduce this pollution, the cone around the B meson is constructed and every particle in this cone is not included in the cone around the leading muon. The size of the cone around B candidate is varied, in order to get the right tracks in cone around muon (still defined as $\Delta R < 0.5$) and the highest tag power. The results (again for both releases) are in the Table 4.9. The tag power rises with increasing number of tracks excluded from the cone around the leading muon. Larger cuts were not tested in order to have sufficient number of tracks in the muon cone. There is also expected that the tag power for larger cuts is smaller than results shown in Table 4.9, Example of cone charge and tag power distribution can be seen in Figures 4.10 and 4.11. The second applied cut is Δz cut (the longitudinal impact parameter of track trajectory relative to primary vertex identified in the event using B-signal candidate). It should help to find and include only those tracks,

Δz	no cut	> 7 mm	> 6 mm	> 5 mm	> 4 mm	> 3 mm
$P_{tag}(\%)$	0.984	1.035	1.036	1.037	1.061	1.059
$P_{tag}(\%)$	1.312	1.311	1.311	1.310	1.318	1.321

Table 4.10: The Δz cut between B candidate and tracks in the muon cone. The $\Delta z > 4$ mm cut means that all track with distance to B candidate bigger than 4 mm are excluded from the cone around the leading muon. Results for release 20.7 results are shown on the first line, results for release 21 on the second one.

which are close to B candidate. The situation is similar to the ΔR cut, the tag power rises with decreasing number of tracks in the muon cone, as is shown in Table 4.10. Again, larger cuts were not tested in order to have sufficient number of track in the muon cone.
To conclude, the κ variation does not help as much as needed. Both ΔR and Δz cuts help, the tag power is increased with any of these cuts applied. Applying both cuts together, $|\Delta z| < 3$ mm and $\Delta R < 0.5$ between tracks in muon cone and the B candidate, the final tag power is $P_{tag} = (1.42 \pm 0.02)$ %, where the error is statistical error and it was calculated as the sum of the square of weights per bin. Final plots of the cone charge and the tag power are shown in Figures . Comparing this value to Tables 4.9 and 4.10, there is a possibility, that these two cuts are correlated. However, it has not been tested yet.

4.6 Tag probability

The main purpose of the study of $B^{\pm} \to J/\psi K^{\pm}$ is to get the probability distribution for tagging. This distribution is used in the main analysis as the calibration distribution.
The probability of B^+ tagging for each passed event is calculated using the formula

$$P(B|Q) = \frac{P(Q|B^+)}{P(Q|B^+) + P(Q|B^-)} \tag{4.10}$$

where $P(Q|B^+)$ is the cone charge value of the B^+ for the specific event and the $P(Q|B^-)$ is the cone charge value of the B^- for the same event. There is no need to construct the probability distribution function of B^- tagging, because these two probabilities are related by $P(\bar{B}|Q) = 1 - P(B|Q)$. The probability distribution is shown in Figure 4.12. The tag probability has been produced separately for muons with tracks in a cone (left plot) and for muon without tracks in the cone.
These probabilities were fitted. The single muon was fitted by two constant functions, the probability for muon cone (with at least one more additional track) was fitted by polynomial funtion of the fourth order. Parameter values of both functions are shown in

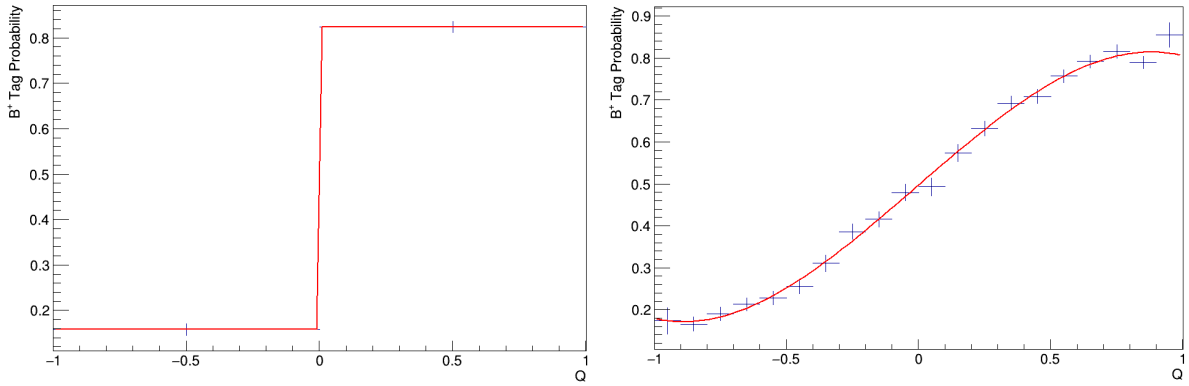

Figure 4.12: The probability distribution for tagged muons, separated into single-track events (left) and cone-charge (right).

	c_1	c_2
value	0.18	0.82
uncertainty	0.03	0.03

p_0	p_1	p_2	p_3	p_4
0.4970	0.520	-0.02	-0.221	0.02
0.0005	0.006	0.01	0.008	0.01

Table 4.11: Left table shows values and errors of the fit parameters presented in the left Figure 4.12 (two constant functions), the right table shows values and errors of the fit parameters presented in the left Figure 4.12 (fourth order polynomial function).

the Table. 4.11.
There exist other flavour tagging methods, for example using electrons or jets instead of muons. In case of doubly tagged event, the tagger with highest tag power is used (usually the muon, electrons have tag power approximately 0.3% comparing to muons tag power of 1.42%, jets have not been tested yet). In case there is no possibility to provide tagging response for the event, then a probability of 0.5 is assigned.

4.7 Using tag information in the B_s^0 fit

The study of the tag power and its sensitivity to each of the cuts described in sections 4.4 and 4.5 has been made in order to find the best cuts. Then, these cuts were applied on muons and tracks in muon cone within the construction of the muon cone charge in B_s^0. The B_s^0 cone charge distribution is shown in Figure 4.13, where peaks with cone charge $Q = \pm 1$ were removed, since they will by applied in the B_s^0 main fit in different way.

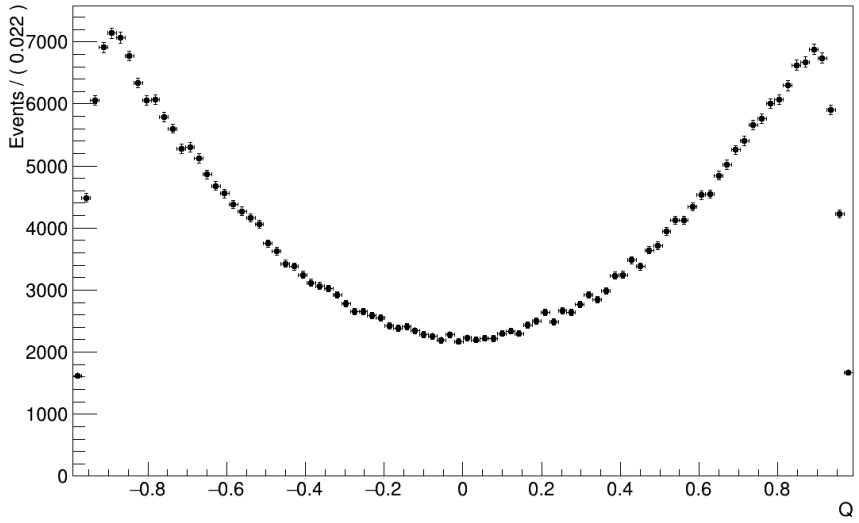

Figure 4.13: B_s^0 cone charge distribution. Peaks with cone charge values $Q = \pm 1$ have been removed, they will by applied in the B_s^0 main fit in different way than this continuous distribution.

The B_s^0 tag probability is extracted from the B_s^0 cone charge (Figure 4.13) and the calibration distribution - the B^+ tag probability (left Figure 4.12). In each tagged event, the B_s^0 cone charge is calculated (and cone charge values $Q = \pm 1$ are not used). Then, this value is put into the function of B^+ tag probability fit. The B_s tag probability is equal to the B^+ tag probability fit function value at the point of calculated B_s^0 cone charge. The B_s^0 tag probability distribution is presented in Figure 4.14.

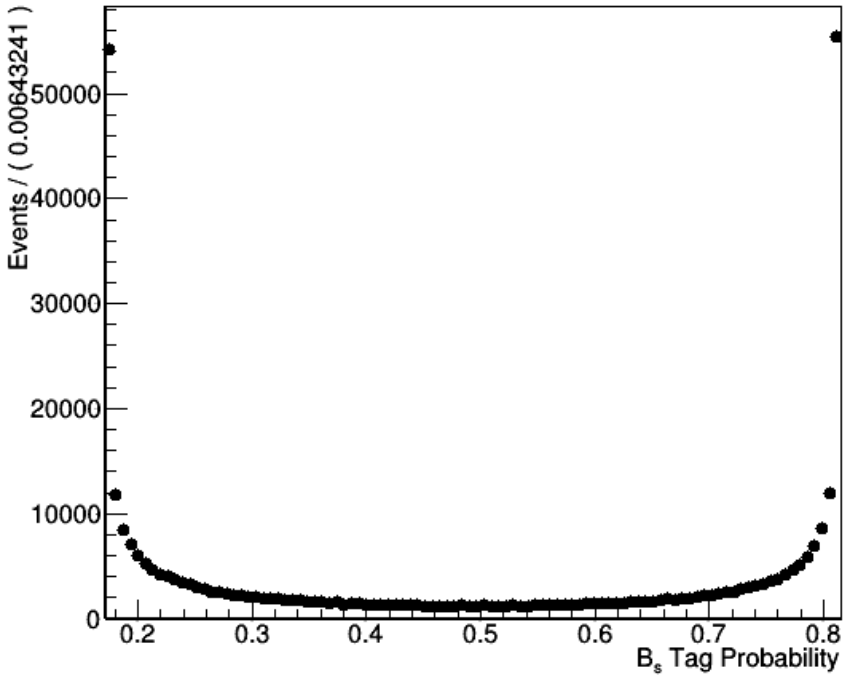

Figure 4.14: B_s^0 tag probability distribution. High number of B_s^0 candidates with high and low tagging probability (approximately 0.8 and 0.2) will has assistant role during the main fit of the function 2.12, because the untagged B_s^0 candidates has default tag probability 0.5 and it is unknown, whether it is B_s^0 or $\bar{B}_s^0$.

Conclusions

This thesis is devoted to the study of the calibration of the B_s^0 opposite side tagging, providing the tag power (information about the strength and quality of tagging). For this purpose, the data from the proton-proton collisions with the center-of-mass energy of $\sqrt{s} = 13$ TeV were used. These data were recorded by the ATLAS experiment at the LHC during the whole year 2016.

The most important of this thesis is the data flow and the description of my own analysis. After testing and applying sets of cuts, the tag power for single muons is $P_{tag} = 0.996\%$ for software release 20.7 and $P_{tag} = 1.32\%$ for software release 21. Applying the cone around the muon and computing the tag values for cone charge, the tag power is $P_{tag} = (1.42 \pm 0.02)\,\%$ (release 21). This demonstrates the improvement of the charge tagging between Run-2 and Run-1 (presented in [28]).

To calibrate the tagging in B_s^0 decays, the B^+ tag probability has been used, see Figure 4.12. Cuts mentioned in 4.4 and 4.5 were applied on muons and tracks in muon cone within the construction of the muon cone charge in B_s^0. The B_s^0 cone charge distribution is shown in Figure 4.13, where peaks with cone charge $Q = \pm 1$ were removed, they will by applied in the B_s^0 main fit in different way.

The next step is to fit the signal part of distribution in Figure 4.13 or 4.14 to obtain Punzi's terms, which will be included in the main fit of the differential branching ratio. Also the calculation of the systematic errors is will be done.

Bibliography

[1] K.A. Olive et al. (Particle Data Group), Chin. Phys. C, 38, 090001 (2014) and 2015 update

[2] Perkins, Donald. Introduction to High Energy Physics. Cambridge University Press, 2000

[3] B. P. Abbott et al., Phys. Rev. Lett., 116, 061102 (2016).

[4] C. W. Misner, K. S. Thorne, J. A. Wheeler. Gravitation. W. H. Freeman and Company,2002.

[5] Barry R. Holstein. Graviton Physics, arXiv:gr-qc/0607045v1, (2006).

[6] W. Pauli letter of the 4th of December 1930, Pauli Archive at CERN.

[7] P. A. R. Ade et al. Planck 2015 results. XIII. Cosmological parameters, arXiv:1502.01589v2, 2015

[8] G. Zweig, An SU(3) Model For Strong Interaction Symmetry And Its Breaking. 2, CERN-TH-412

[9] M. Gell-Mann, Phys. Lett. 8, 214 (1964).

[10] J. J. Aubert et al., Phys. Rev. Lett. 33, 1402 (1974).

[11] S. W. Herb et al., Phys. Rev. Lett. 39, 252 (1977).

[12] S. F. Abe et al., Phys. Rev. Lett. 74, 2626 (1995).

[13] P. A. R. Ade et al. Planck 2015 results. XIII. Cosmological parameters, arXiv:1502.01589v2, 2015

[14] R. Aaij et al., Phys. Rev. Lett., 112, 222002 (2014).

[15] R. Aaij et al., Phys. Rev. Lett.,115, 072001 (2015).

[16] P. A. M. Dirac, "A Theory of Electrons and Protons," Proc. Roy. Soc. A126, 360 (1930).

[17] C. S. Wu, E. Ambler, R. W. Hayward, D. D. Hoppes, R. P. Hudson, Phys. Rev. Lett, 105, 1413-1415 (1957).

[18] Angelopoulos et el., Phys. Lett. B 444, 43-51 (1998).

[19] J. H. Christenson, J. W. Cronin, V. L. Fitch, and R. Turlay, Phys. Rev. Lett. 33, 138 (1964).

[20] B. Aubert et al., Phys. Rev. Lett. 100, 131802 (2008).

[21] R. Bluhm, Nucl. Instrum. Methods Phys. Res., B 221, 6-11 (2004).

[22] The KLOE-2 Collaboration, Phys. Lett. B 730, 89-94 (2014).

[23] N. Cabibbo, Phys. Rev. Lett. 10, 531 (1963).

[24] M. Battaglia et al., The CKM Matrix and the Unitarity Triangle, arXiv:hep-ph/0304132.

[25] CKMfitter group,The global CKM fit in the small (ρ-bar,η-bar) plane, accessed 17. 9. 2017 [Online]. Available at `http://ckmfitter.in2p3.fr/www/results/plots_ichep16/ckm_res_ichep16.html`

[26] Y. Nir, H.R. Quinn, Annu. Rev. Nucl. Part. Sci. 42 (1992), 211.

[27] R.Aaij et al., Phys. Lett. B 736 (2014).

[28] G. Aad et al., Journal of High Energy Physics, No. 8, 147, (2016).

[29] V.M. Abazov et al., Phys. Rev. D 85, 032006 (2012).

[30] R. Aaij et al., Phys.Rev.Lett. 108, 241801 (2012).

[31] William Panduro Vazquez, Atlas Data Acquisition: from Run I to Run II, ATLAS Note ATL-DAQ-SLIDE-2014-387 (2014).

[32] The ATLAS Collaboration at al., The atlas experiment at the CERN Large Hadron Collider, Journal of Instrumentation, vol. 3, no. 08, p. S08003, 2008

[33] Carlo Schiavi, ATLAS High-Level Trigger algorithms for Run-2 data-taking, ATLAS Note ATL-DAQ-PROC-2015-018 (2015).

[34] ATLAS Collaboration , Muon reconstruction performance of the ATLAS detector in proton-proton collision data at $\sqrt{s} = 13$ TeV, CERN-EP-2016-033 (2016).

[35] N. Orlando, ATLAS Note ATL-PHYS-PROC-2012-011 (2012).

[36] R. Nicolaidou, L. Chevalier, S. Hassani, J.F. Laporte, E.L. Menedeu, A. Ouraou, J. Phys. Conf. Ser. 219, 032052 (2010).

[37] G. Aad et al., ATL-PHYS-PUB-2015-037 (2015).

[38] http://proj-gaudi.web.cern.ch/proj-gaudi/

[39] R. Brun and F. Rademakers, Nucl. Instrum. Meth. A389 81–86 (1997).

[40] https://root.cern.ch/

[41] http://roofit.sourceforge.net/

[42] M. Pivk and F. R. Le Diberder, Nucl. Instrum. Meth. A555, 356 (2005).